



HAL
open science

Time-reversal in diffusive media

Andrea Cozza, Florian Monsef

► **To cite this version:**

Andrea Cozza, Florian Monsef. Time-reversal in diffusive media. Farhad Rachidi. Electromagnetic Time Reversal: Application to Electromagnetic Compatibility and Power Systems, 2017, 10.1002/9781119142119 . hal-01377943

HAL Id: hal-01377943

<https://centralesupelec.hal.science/hal-01377943v1>

Submitted on 7 Oct 2016

HAL is a multi-disciplinary open access archive for the deposit and dissemination of scientific research documents, whether they are published or not. The documents may come from teaching and research institutions in France or abroad, or from public or private research centers.

L'archive ouverte pluridisciplinaire **HAL**, est destinée au dépôt et à la diffusion de documents scientifiques de niveau recherche, publiés ou non, émanant des établissements d'enseignement et de recherche français ou étrangers, des laboratoires publics ou privés.

7

Time-reversal in diffusive media

A. Cozza, F. Monsef

Group of electrical engineering Paris (GeePs), Gif-sur-Yvette, France

1.1 Introduction

Fog, clouds, matt surfaces, even the human skin. All of them present a strong diffusive behavior. Without it, the sky would be a dull black. When light propagating along a single direction interacts with these diffusive media, it is scattered over a large fan of directions, making fundamentally impossible to understand where light came from in the first place. The next time you drink a glass of milk observe it closely and ask yourself if you can guess where the light that brightens it comes from.

Diffusive media are very common at visible optical frequencies; our brain is so accustomed to them that it fundamentally exploits their signature response as one of the features it uses for classifying surfaces. Switching to acoustics, at audible frequencies we are more comfortable with diffusion than with reflections: just think about how annoying are the separate echoes in a train station and how much we enjoy a concert hall with “good acoustics”, a more common name for perfect diffusion [1, 2].

Enter now microwave frequencies and the concepts introduced by decades of undergraduate courses. Free-space propagation sets the standard, with the odd diffraction coming from a few isolated scatterers presented more as a nuisance than an opportunity, because of their complexity. Single mirror reflections are typically presented as the building block for multipath propagation; wave diffusion is hardly mentioned.

Yet, diffusion is not only important in understanding propagation at optical frequencies. Diffusion actually happens quite often with microwaves, too. As a matter of fact, non-line-of-sight propagation in rooms and urban canyons share some of the characteristics of wave diffusion, which is better known as the class of Rayleigh channels in telecommunication theory [3].

Perhaps more important is the fact that wave diffusion can be useful. Reverberation chambers are the champions of wave diffusion, as their peculiar characteristics heavily depend on the ability to turn coherent excitations into a chaos of waves propagating along (ideally) every possible directions at the same time.

When used as the basis for time reversal applications, diffusive media can be shown to take a whole new dimension that makes them suddenly appear as very appealing media for wave propagation, rather than the messy and uncontrollable medium we are used to expect with harmonic excitations.

This chapter presents a summary of the work done in applying time reversal to diffusive media. It is organized into three parts. First, the main features of diffusive media are presented, starting from their physical origin leading to the derivation of black-box statistical models; these properties will be fundamental in the derivation of the results presented later. Time-reversed excitations are then considered, first for the generation of fields and the transmission of signals. The powerful self-averaging enabled by diffusive media is demystified, proving why it can only happen with such media. Self-averaging powers all of the properties of time reversal in diffusive media, as its ability to generate well-polarized fields in a medium considered as incapable of doing it.

These results are then pushed a step further, by studying the generation of coherent wavefronts. Diffusive media are shown to be a potentially more effective solution for this task than free-space-based wave generators: a single antenna is shown to be capable of generating a large number of focusing wavefronts just by playing on the signals applied to it. Applications presented throughout the chapter are based on the use of reverberation chambers.

1.2 Fundamental properties of diffusive media

Before discussing the applications of time reversal in diffusive media, it is necessary to have at least an intuitive understanding of the physical origin of their properties. These are described in Section 1.2.1, introducing the plane-wave spectrum representation. From these observations, general statistical properties are inferred and used in order to introduce in Section 1.2.2 statistical black-box representations that capture the macroscopic behavior of diffusive media.

1.2.1 *Understanding and describing wave propagation in diffusive media*

The notion of a diffusive medium is associated with environments where waves are submitted to a large (ideally infinite) number of scattering events. Such media go fundamentally under three categories: 1) rough surfaces, where an impinging wave is randomly back-scattered; 2) complex distributions of small scatterers, through which an impinging wave travels, e.g., Rayleigh scattering; 3) multiple scattering of waves generated in a (at least) partially close medium, e.g., indoor environments.

In the context of this chapter, only the third configuration will be considered. In fact, all of the three configurations could be described as discussed in this section and the next one. But the applications presented later refer, at a certain point, to closed media where scattering events are weakly dissipative. This condition is necessary in order to ensure that waves scattered by a portion of the medium boundary will travel to another part of the boundaries and undergo another round of scattering events, and so on for a large number of times. A closed structure without the assumption of weak losses could not support strong diffusion, making the simplified models in Section 1.2.2 too crude.

The coherence of waves propagating in these media is thus broken into small regions of coherence: what would have been an extended wavefront in free space, is reduced to a collection of cells moving randomly in all directions [4, 5], an outcome known as speckle distribution. An example is shown in Figure 1.

Multiple-scattering does not necessarily imply that portions of the original energy propagate along every possible directions; media such as tunnels with cross-sections

covering several wavelength present diffusion, but mainly across a reduced set of directions, since the average energy it conveys moves longitudinally.

The simplest representation that can be picked up for all of these configurations is the plane-wave spectrum [6]. It is widely used across all disciplines involving wave propagation, from acoustics to optics and even in quantum mechanics, taking a variety of names, as reciprocal-space representation or Fourier optics.

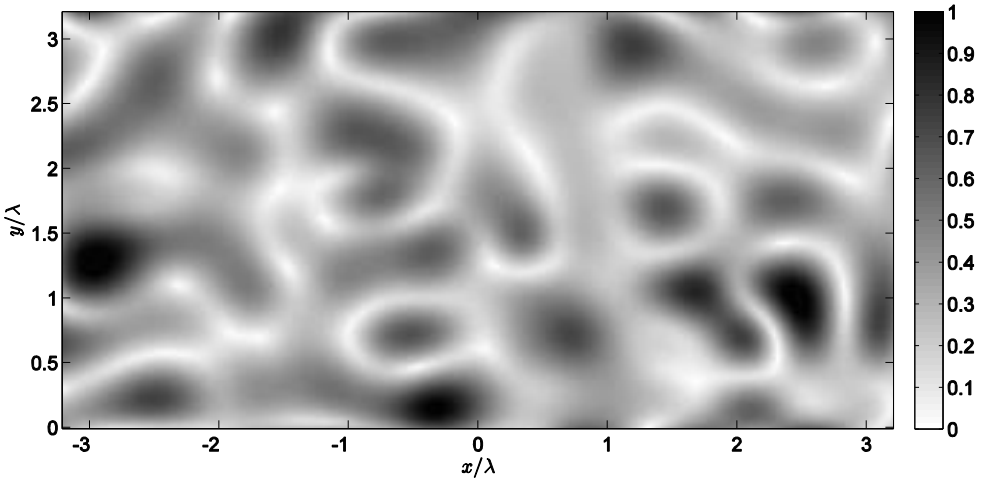


Figure 1 : An example of spatial speckle (amplitude) distribution generated by a superposition of randomly excited plane waves. Nodal surfaces, shown in white, delimit coherent cells about half-wavelength wide.

In fact, it is just an extension of Fourier transform, applied to space rather than time. The following definition of the plane-wave spectrum $\tilde{\mathbf{E}}(\mathbf{k}, \nu)$ will be used

$$\mathbf{E}(\mathbf{r}, \nu) = \int d\mathbf{k} \tilde{\mathbf{E}}(\mathbf{k}, \nu) e^{-j\mathbf{k} \cdot \mathbf{r}} \quad (1)$$

to represent a field distribution $\mathbf{E}(\mathbf{r}, \nu)$, where \mathbf{k} is the propagation vector of each plane wave on which the spatial field distribution is expanded; ν is the frequency at which the plane-wave spectrum is defined for an harmonic excitation. Depending on the propagation mechanisms involved, $\tilde{\mathbf{E}}(\mathbf{k}, \nu)$ can be a deterministic or a (partially) random function. Section 1.2.2 will only consider random plane-wave spectra.

Why should we be interested in random representations? Essentially because deterministic descriptions are possible but often unlikely or untreatable. Two reasons can be given about the need of random representations of field distributions in reverberation chambers: 1) their Green functions are highly complex and even numerical solutions are cumbersome, due to the resonant nature of these media; 2) reverberation chambers basically work as interferometers, therefore the field distributions they generate are very sensitive to the geometry and nature of their boundaries. In practice, the solutions sought for reverberation chambers do not imply a perfect knowledge of their fields at any position in a deterministic way, but more of a macroscopic evaluation of their performance. An example is given by the need to know the average field level a reverberation chamber can generate, with no need to know where (and even if) this specific value of field will appear. Hence the statistical description used for electromagnetic reverberation chambers [7, 8] predated by the work done in acoustics [9, 10, 11, 12].

The reasons and motivations given above retrace those considered in the development of the kinetic theory of gases, pioneered by J.C. Maxwell and L.E. Boltzmann [13]. Coherently with this mindset, rather than looking for spatial solutions of fields generated by reverberation chambers (or any diffusive media), we rather need to start by arguing about the properties that should be expected for their plane-wave spectra and work our way back to understand spatial properties, as done in Section 1.2.2.

The assumption of perfect diffusion will be the cornerstone of this entire chapter. It requires that energy is randomly distributed along all possible directions, with equal probability and average intensity. The concept of probability is here defined across all possible realizations of field distributions (ensemble), not only the single distribution one could experience in a given configuration. Furthermore, for each direction, energy can be associated to any polarization for the electromagnetic field; e.g., this condition is used in optics to describe incoherent light.

Why should we expect these conditions to hold in practice? Fundamentally, there is no demonstration for their validity, as it would require the existence of exact solutions serving as references. The validity of these conditions are always validated a posteriori against experimental results. Qualitative reasons usually given for these assumptions are that the field radiated by a source within these media undergoes a number of scattering events that redistribute energy across an ever larger number of directions. Moreover, the fact that these chambers are electrically large, implies that

along any direction of propagation delay translates into uniformly random phase-shift angles. These two conditions are practically sufficient to invoke the concept of diffuse-field propagation.

From acoustics to electromagnetics, it appears to give satisfaction as soon as a large number of degrees of freedom are accessible at the same time. Without going into details, reverberation chambers need to be electrically large and present a certain degree of losses [14, 2].

If the field at any position is the result of a large number of random and independent plane waves, then the central limit theorem states that the field should asymptotically behave as a Gaussian random variable. The link between a random superposition of independent contributions and Gaussianity goes back to the earliest works on Brownian motion [15].

Diffusion has implications on the time-domain responses, too. A receiver within a diffusive medium would initially record only a few distinguishable echoes which, as time passes and multiple scattering events take place, let an ever larger number of smaller and superposed echoes appear. The result is what is commonly known as reverberation, a phenomenon apparent at acoustical frequencies in large bounded environments like empty hangars and cathedrals. For our purposes, reverberation is important as it implies that exciting a diffusive medium with a short pulse, its response can be several orders of magnitude longer, as discussed in Section 1.3.1. A pulse can be deformed in this way only if its frequency components are made incoherent, i.e., they appear to have both amplitude and phase-shift angles behaving as independent random variables. As an example, one of the reverberation chambers in our department responds with a time constant of about 3 μs , despite the fact that line-of-sight propagation through it just takes 20 ns, implying a very large number of interactions over its boundaries.

This condition leads to another fundamental property of diffusive media. Wiener-Khinchin theorem implies that random-like impulse responses with energy distributions that fade very slowly are underpinned by narrow coherence bandwidths. In other words, the longer the decay time, the more incoherent the frequency response, and thus richer in degrees of freedom that can be excited independently one from the other.

The broad picture evinced from these observations is that of a class of media that could hardly be expected to support coherent propagation of waves. As it will be

shown in the rest of this chapter, time reversal can completely revert this expectation, making diffusive media appealing for coherent applications.

1.2.2 Statistical black-box modelling

The assumption of perfect diffusion can be translated into a number of macroscopic properties shared, at least approximately, by all diffusive media. The approximate nature of this approach comes from the impossibility to ensure an infinite number of degrees of freedom. Statistical moments are the language we need and they are applied across all possible random realizations, by computing averages, indicated as $\langle \cdot \rangle$.

Perfect diffusion can be stated very succinctly using a plane-wave spectrum description

$$\langle \tilde{\mathbf{E}}^H(\mathbf{k}_i) \cdot \tilde{\mathbf{E}}(\mathbf{k}_j) \rangle = \tilde{E}_o^2 \delta_{ij} \quad (2)$$

where $\tilde{\mathbf{E}}(\mathbf{k}_i)$ is the plane-wave spectrum of a field distribution, say the electric field, sampled at the wavenumber \mathbf{k}_i . Eq. (2) includes angular uniformity of the spectral power density \tilde{E}_o^2 , uncorrelation of the individual plane-wave contributions and depolarization.

The other assumption behind perfect diffusion is a uniform probability for all phase-shift angles of the plane waves. Their amplitudes just need to be random and although they can be expected to be zero-averaged, this condition has no impact on the corresponding spatial properties.

The first property that can be derived from these two conditions is the covariance of the spatial field. Defined as

$$\mathbf{C}_E(\mathbf{r}) = \langle \mathbf{E}^H(\mathbf{r}) \cdot \mathbf{E}(\mathbf{r}) \rangle = \frac{\langle |\mathbf{E}(\mathbf{r})|^2 \rangle}{3} \mathbf{1} = \frac{E_o^2}{3} \mathbf{1} \quad (3)$$

it results in a spatial field distribution whose scalar components are uncorrelated and share the same average intensity $E_o^2/3$ which also appears to be constant across space (homogeneity); $\mathbf{1}$ is the identity matrix.

When comparing field samples observed at different positions, correlations can be computed, in order to evaluate if the field samples are somehow coupled or not. This is the analog of assessing whether a time-series has memory.

The spatial correlation coefficient, the normalized definition of spatial correlation, is found to be

$$\mu_r(|\mathbf{r}_1 - \mathbf{r}_2|, \nu) = \frac{\langle \mathbf{E}^H(\mathbf{r}_1, \nu) \cdot \mathbf{E}(\mathbf{r}_2, \nu) \rangle}{E_0^2} = \text{sinc}(k|\mathbf{r}_1 - \mathbf{r}_2|) \quad (4)$$

thus mostly concentrated in a region about half a wavelength wide, consistently with the qualitative observations in the speckle distribution in Figure 1. This is just one of the possible spatial correlation functions that can define the macroscopic behavior of diffusive media [16].

The frequency-domain behavior is mainly characterized by means of a correlation function

$$\mu_\nu(|\nu_1 - \nu_2|) = \langle \mathbf{E}^H(\mathbf{r}, \nu_1) \cdot \mathbf{E}(\mathbf{r}, \nu_2) \rangle / E_0^2 \quad (5)$$

with a typical scale of correlation summarized by the coherence bandwidth

$$B_c = \int d\Delta\nu \mu_\nu(\Delta\nu) \quad (6)$$

which is related to the average decay time, or relaxation time, τ of the medium as

$$\tau = 1/B_c \quad (7)$$

Clearly, high-order statistics have been studied, but what has been presented in this section is the minimum set of properties needed in order to understand how time reversal works in diffusive media.

1.3 Time-reversal transmissions in diffusive media

Suppose a transmitter is used in a diffusive medium in order to reproduce a signal $p(t)$ at the receiver end, or equivalently a field at a given position, later also referred to as the target signal or pulse, with $P(\nu)$ its corresponding Fourier spectrum. If $H(\nu)$ is the transfer function between transmitter and receiver, then directly applying $p(t)$ to the transmitter would result in the reception of an incoherent signal, since its spectrum $P(\nu)H(\nu)$ has lost any resemblance of the frequency coherence that characterized the spectrum of the originally intended signal $p(t)$. The reason behind this claim is to be found in the statistical properties of diffusive media, as recalled in Section 1.2.2: $H(\nu)$ has a short coherence bandwidth, outside which it behaves as an independent random function that will therefore act as random weights on $P(\nu)$. As a result, portions of $P(\nu)$ that were meant to be in phase and with slow amplitude variations will inherit the fast and random frequency variations of $H(\nu)$, yielding a received signal affected by long spread times.

Time reversal, in its original definition, provides a solution that is essentially equivalent to a matched filter, applying a signal $x(t)$ with a spectrum

$$X(\nu) = P(\nu)H^*(\nu) \tag{8}$$

to the transmitter, thus receiving a signal $y(t)$ with a spectrum

$$Y(\nu) = P(\nu)|H(\nu)|^2 \tag{9}$$

The Fourier spectrum in (8) corresponds to the time-reversed version of the signal received by the receiving antenna. Because of this operation, it is often referred to as a time-reversal mirror, or TRM.

Depending on the class of propagation medium, the received signal may have very different properties. Free-space propagation, and in general open media where line-of-sight propagation is a good approximation, implies that $|H(\nu)|^2$ is mostly flat or very slowly varying, so that it is reasonable to expect $Y(\nu) \propto P(\nu)$, i.e., a practically perfect transmission of the target signal $p(t)$ that was meant to be transmitted.

A very different behavior is observed in diffusive media. In Section 1.2.2 their frequency responses were shown to be affected by fast variations, with a scale of variation captured by their coherence bandwidth B_c . In case $P(\nu)$ spans a bandwidth $B_T \gg B_c$, (9) would be dominated by the variations in amplitude of the transfer function, profoundly modifying the original shape of $P(\nu)$. Eq. (9) ideally removes the possibility of destructive interference, since phase shifts are equalized to zero for all frequencies. In effect, the original envelope on the target spectrum is hardly recognizable in $Y(\nu)$, as clear in Figure 2.

Still, time-reversal transmissions can be effective and lead to good transmissions of target signals at the receiver. The secret behind their effectiveness is qualitatively explained in 1.3.1 and later given a more demonstration in Section 1.3.3.

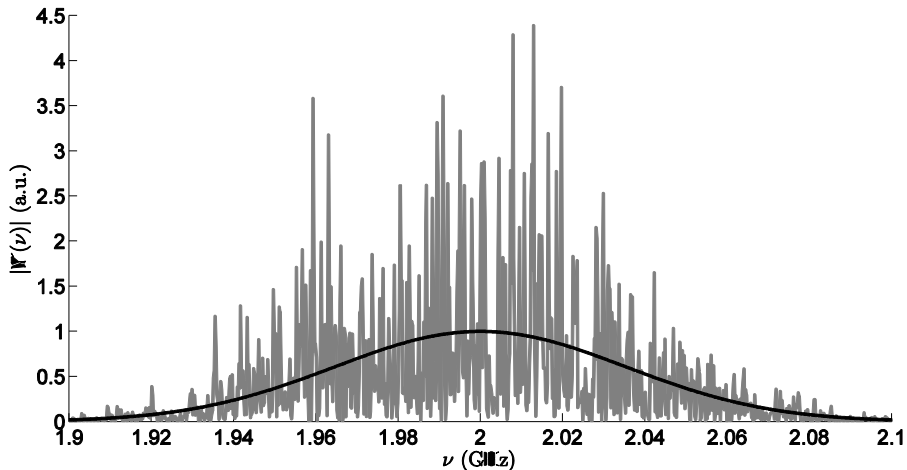


Figure 2 : An example of received spectrum $Y(\nu)$ (amplitude shown in grey color), for a Gaussian target spectrum $P(\nu)$ (black line): the target Gaussian profile is hardly recognizable.

1.3.1 Self-averaging and spectral coherence

Self-averaging is likely the most impressive feature of time-reversal applications in diffusive media [17, 18, 19]. In the previous section it was argued that the spectrum of signal transmitted with time reversal are so strongly modified by low frequency

coherence of the medium that it is surprising that back in the time domain these signals actually appear to be good replicas of a target signal.

Figure 3 provides a qualitative example of time-reversal performance in diffusive media. A medium with an impulse response thousands of times longer than the signal to transmit can generate a short pulse at the output of a receiver. These results only let appreciate the time compression enabled by time reversal; the spatial counterpart of this compression will be discussed in Section 1.4.

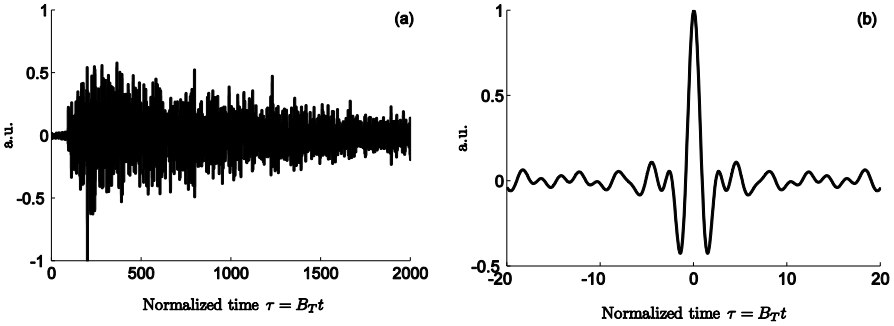


Figure 3 : An example of impulse responses measured in one of CentraleSupélec’s reverberation chambers, for $f_c = 1.1$ GHz and $B_T = 0.5$ GHz: (a) direct impulse response $h(t)$ and (b) equivalent impulse response $h(t) \star h(-t)$ for time-reversal transmissions. Time is normalized to the coherence time $1/B_T$.

There exist several ways of exposing and understanding self-averaging. We propose to start from the time-domain representation of the received signal $y(t)$

$$y(t) = p(t) \star h(-t) \star h(t) \tag{10}$$

with $h(t)$ the impulse response of the propagation medium and \star the convolution operator applied to the time variable. The portion $y(-t) \star y(t)$ is a short step away of the autocorrelation function $R_{hh}(t)$ of the impulse response, defined as

$$R_{hh}(t) = \langle h(-t) \star h(t) \rangle \tag{11}$$

for $h(t)$ interpreted as a random process. It is worth relating the autocorrelation function of $h(t)$ to the received signal

$$\langle y(t) \rangle = p(t) \star R_{hh}(t) \quad (12)$$

as it has something to tell about the potential outcome of time-reversal transmissions.

In this last equation, the ensemble average of an *infinite* set of signals received in a given medium corresponds to the convolution of the target signal with $R_{hh}(t)$. Depending on whether $R_{hh}(t)$ distorts $p(t)$ or not, signals could be perfectly received, at least on average.

This would be a best-case that is therefore worth studying. It can be done more easily in the frequency domain, by recalling Wiener-Khinchin theorem

$$R_{hh}(t) = \int_{B_T} d\nu \langle |H(\nu)|^2 \rangle e^{j2\pi t \nu} . \quad (13)$$

Assuming that the random process $H(\nu)$ follows a Gaussian law $N(0, \sigma_H(\nu))$, as reasonable for diffusive media (see Section 1.2), it is clear that in order to have $\langle y(t) \rangle \propto p(t)$, $\sigma_H(\nu)$ needs to be constant over the bandwidth B_T of $p(t)$; otherwise a distortion would appear, as $P(\nu)$ would then be weighted unequally.

Although this observation implies that time reversal transmissions can potentially be perfect on average, in practice only one realization is available per transmitter. It is therefore fundamental to understand how close (10) is to (12), by studying

$$\Delta y(t) = y(t) - \langle y(t) \rangle = \int_{B_T} d\nu P(\nu) [W(\nu) - \langle W(\nu) \rangle] e^{j2\pi \nu t} \quad (14)$$

having introduced the time-reversal transfer function $W(\nu) = |H(\nu)|^2$. It is now clear that fluctuations in received signal are due to deviations of $W(\nu)$ from its average value. Hence, as a medium gets more complex and multipath contributions get to interfere, its transfer functions can present local deviations from line-of-sight behavior, which is essentially flat in the frequency domain.

Back to (14), the random process $W'(\nu) = W(\nu) - \langle W(\nu) \rangle$ is now centered, i.e., zero-averaged. Eq. (14) can be written as

$$\Delta y(t) = \sum_{n=1}^N \int_{B_n} dv P(v) W'(v) e^{j2\pi vt} \simeq \sum_{n=1}^N P(v_n) \int_{B_n} dv W'(v) e^{j2\pi vt} \quad (15)$$

where the sub-bandwidths B_n are chosen to be identical over the entire bandwidth B_T , so that $N = B_T/B_n$. If B_n is small enough, $P(v)$ can be regarded as constant over B_n , hence the above approximation, where v_n is the central frequency of each sub-bandwidth B_n .

Eq. (15) can be restated as

$$\Delta y(t) \simeq \sum_{n=1}^N P(v_n) G_n \quad (16)$$

where G_n (implicitly defined) behave as random variables. If B_n is chosen such that the G_n are independent and identically distributed, (16) can be simplified as explained just below. This condition depends on the integrands in (15), and therefore on the time t at which they are evaluated. For pulsed signals, most of their energy is found for $|t| < 1/B_T$. In this case, the phase shifts introduced by the Fourier kernel $e^{j2\pi vt}$ in (15) can be regarded as negligible over a number of adjacent sub-bandwidths. As a result, the G_n can be expected to be independent and identically distributed as soon as $B_n \geq B_c$. Since $H(v)$ fluctuates on a very short scale when compared to $P(v)$, this last condition is compatible with the idea of seeing $P(v)$ as constant over B_n .

Interpreting (16) as a weighted average of the G_n , i.e., of random variables, the central limit theorem can be invoked. Having chosen the B_n to ensure independence of the G_n , this theorem can be applied, concluding that the random variable $\Delta y(t)$ asymptotically follows a Gaussian distribution, centered around zero and with a standard deviation that scales as $1/\sqrt{B_T/B_c} = 1/\sqrt{N}$.

To make a long story short, time-reversed signals in diffusive media start to substantially converge to a target signal as soon as N exceeds 100. In diffusive media B_c can be very small; e.g., in a reverberation chamber operated at 1 GHz with a quality factor around 10^4 , $B_c \simeq 300\text{KHz}$, hence a good convergence can be expected for $B_T > 30\text{ MHz}$, i.e., a fractional bandwidth of just 3 %. This result is in

sharp contrast with the bandwidths displayed in acoustics, where fractional bandwidths exceeding 50 % are often used without a clear justification [20, 21].

More details about the performance of time-reversal transmission in diffusive media are presented in Sections 1.3.3 and 1.3.5, in particular about quantitative predictions of the accuracy of the received signals.

As a final remark about self-averaging in diffusive media, it is interesting to ponder the following question when looking at (12): what properties $h(t)$ needs in order for its autocorrelation function not to modify $p(t)$? Not modifying a band-limited function requires that $R_{hh}(t)$ be proportional to a cardinal sine (or sinc) function, with a Fourier spectrum spanning a frequency bandwidth containing that of $p(t)$, i.e., B_T . This condition is met in two extreme cases : a perfect channel that does not modify a signal or, paradoxically, one that has an impulse response behaving as a white noise, at least over B_T . In fact, diffusive media, as recalled in Section 1.2.2 do have impulse responses that resemble Gaussian random processes. It is therefore fitting to conclude that the most complex media that nature can produce can behave as the simplest one, once time-reversed signals are applied to them. This could also be seen as a further application of Van Cittert – Zernicke theorem [22], where random processes can lead, under certain conditions, to deterministic outcomes.

1.3.2 *Taking a broader view: spatial speckle and background fluctuations*

The previous section has highlighted a direct cause-effect link between rapid variations in transfer functions in diffusive media and random fluctuations in time-reversal transmissions, underpinned by a Fourier transform.

The same idea can be applied to another important couple of quantities also constituting a Fourier pair: spatial and angular field distributions. In fact time reversal is not only a way of compressing time signals, but operates on both the space and time evolution of a wavefront as two facets of a single physical phenomenon. These two aspects should not be separated or regarded as independent.

While details about time-reversed wavefronts in diffusive media are given in Section 1.4, here we just want to give a preliminary discussion about why and how time-reversed wavefronts always appear as moving through a sort of noisy background. In the same way that the received and target signals are related by a convolution kernel,

also the spatial distribution of a time-reversed wavefront and the reference distribution moving through free-space are related by a convolution kernel, even though more complex.

When this convolution is recast in its Fourier-transformed version, space is supplanted by directions of propagation of what could be interpreted as plane waves. Hence, as in the previous section, rapid variations in the propagation operator must lead to fluctuations in the spatial distribution of time-reversed fields.

Why should one expect rapid variations in the propagation operator? And what ultimately is this operator standing for? A spectral point of view was already presented in Section 1.2, and basically models the fact that propagation within diffusive media, because of their boundary conditions, mostly happens along certain directions, and more importantly, with a varying intensity, due to constructive and destructive interference between multipath contributions.

Hence, there is no point in expecting time-reversed wavefronts to be free of background fluctuations, which typically take the shape of a speckle distribution, as defined in Section 1.2.1.

The intimate connection between spatial and time fluctuations can be evidenced by recalling that a receiving antenna fundamentally acts as a spatial (and partially angular) sampler [23]. In the simplest case, its output signals are just a copy of the fields found at its position. Therefore, in this simplified example, spatial fluctuations in the field distribution and time fluctuations in the received signal are the same. If the antenna has a marked directivity, than the two sets of fluctuations can differ, although their evolutions are still strongly related.

1.3.3 How accurate are time-reversed fields in diffusive media?

Signals, and also fields, generated by time reversal in diffusive media are not perfect; even worse, they have a random nature. Their accuracy can be measured, and ultimately predicted, by knowing just a few statistical metrics of the medium.

The first step is to define what is meant by accuracy. Since received signals are expected to get as close as possible to a target signals, it is possible to represent received signals as [24]

$$y(t) = \alpha p(t) + f(t) \quad (17)$$

i.e., as a partial perfect transmission of the target signal and a random process $f(t)$. In order to cover the most general scenarios, several transmitting antennas are supposed to take part to the transmission. Therefore, in general

$$y(t) = \sum_m^{N_A} \alpha_m p(t) + \sum_m^{N_A} f_m(t) \quad (18)$$

where N_A is the number of antennas. For each antenna a transfer function $H_m(\nu)$ can be defined between the transmitting and receiving antenna. The coefficients α_m can be computed by projections, e.g., in the frequency domain,

$$\alpha_m = E_p^{-1} \int_{B_T} d\nu W_m(\nu) |P(\nu)|^2 \quad (19)$$

with $W_m(\nu) = |H_m(\nu)|^2$ the time-reversal transfer function and E_p the mathematical energy of the target signal. Given that the functions in the integrand are positive defined, the coefficients $\alpha_m \geq 0$ by definition. Therefore multiple-antenna time-reversal transmissions cannot interfere destructively.

From (18) the accuracy of time reversal can be measured as the contrast between the coherent and incoherent contributions

$$\Lambda_p = \frac{\alpha^2 p^2(0)}{\max_t \langle f^2(t) \rangle} \quad (20)$$

having assumed, with no loss of generality, that the peak of the target signal is reached at $t = 0$. The above definition will be referred to as peak contrast as it is based on peak powers for the coherent (instantaneous power) and incoherent (average power).

The peak contrast can be factorized by introducing the shape factors

$$\chi_p = \frac{|p(0)|^2}{E_p} \quad (21)$$

$$\chi_f = \frac{\max_t \langle f^2(t) \rangle}{\langle E_f \rangle}$$

which measure the coherences bandwidth of the target signal and incoherent fluctuations; (20) can now be expressed

$$\Lambda_p = \Lambda \frac{\chi_p}{\chi_f} \quad (22)$$

with

$$\Lambda = \frac{E_c}{E_f} = \frac{\alpha^2 E_p}{\int_{B_T} dv |F(v)|^2} \quad (23)$$

the energy contrast, which now measures the ratio of the coherent and incoherent energies. The rationale behind this factorization is that it is possible to prove [25] that Λ only depends on the statistical properties of the medium, and not those of the target signal. The derivation of an explicit relationship between Λ and the medium statistical properties is cumbersome and therefore cannot be reproduced here. The result derived in [25] proves that

$$\langle \Lambda \rangle \simeq \varsigma_W^{-2}(v_c) D(N_A, \bar{\mu}_r) \quad (24)$$

with

$$\varsigma_W^2(v) = \frac{\sigma_W^2}{\langle W(v) \rangle^2} \quad (25)$$

the statistical variability of the time-reversal transfer function, i.e., whose square-root value measures how strongly $W(v)$ can deviate from its average value. For perfectly diffuse fields, it is equal to 1. The other term in (24) is the diversity factor,

$$D(N_A, \bar{\mu}_r) = \frac{N_A}{1 + (N_A - 1)\bar{\mu}_r} \quad (26)$$

which measures the effective number of degrees of freedom introduced by the N_A transmission antennas, for an average correlation coefficient $\bar{\mu}_r$ between the $W_m(\nu)$ time-reversal transfer functions.

Two conclusions can be drawn. First, the medium itself sets a scale of the performance of time-reversal transmissions. While the peak contrast Λ_p can be controlled by acting on the bandwidth of the excitation signal, the fraction of received energy associated to target signal is definitely fixed by the medium.

Second, having several antennas cooperating to the transmission can help, since the diversity factor $D(N_A, \bar{\mu}_r) \geq 1$. So using time-reversal mirrors in diffusive media still makes sense, even though not for the same reasons as in open media, i.e., not in order to define a time-reversal cavity (e.g., an Huygens' surface). But depending on the independence of the time-reversal transfer functions $W_m(\nu)$, adding antennas could represent an ineffective solution. $D(N_A, \bar{\mu}_r)$ is plotted in Figure 4, where it is clear that as soon as a small average correlation appears, the increase in the energy coherence is reduced. This reduction is stronger as the number of antennas already present increases. Since correlations around 20 % are all but rare, multiple-source configurations can be costly, as they risk bringing very minor improvements while forcing the need for synchronized excitations. This last point has practical importance, since synchronized generation of multiple wideband signals is a far from an obvious task.

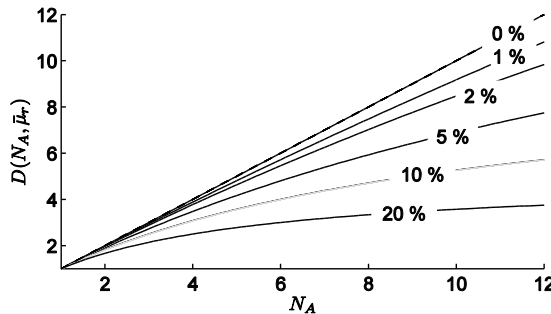


Figure 4 : The diversity factor $D(N_A, \bar{\mu}_r)$ as a function of the number of sources N_A and the average spatial degree of coherence $\bar{\mu}_r$ in percent units over each curve.

As just recalled, while Λ can be difficult and costly to control, (22) states that the peak contrast does not only depend on the medium through χ_f , but can also be modulated by accurately designing the target signal, acting on χ_p . Eq. (22) can be made clearer by noticing that the two shape factors can be expressed in terms of characteristic time constants: e.g., $\chi_f \propto 1/T_f$, with T_f is the relaxation time of the medium, i.e., the time constant of its root-mean-square impulse response; in a similar way, $\chi_p \propto 1/T_p$, with T_p the time support of the target pulse, e.g., defined as the portion of pulse containing half of its energy or where the pulse passes to half of its peak power. Hence making the target signal shorter makes the peak contrast increase.

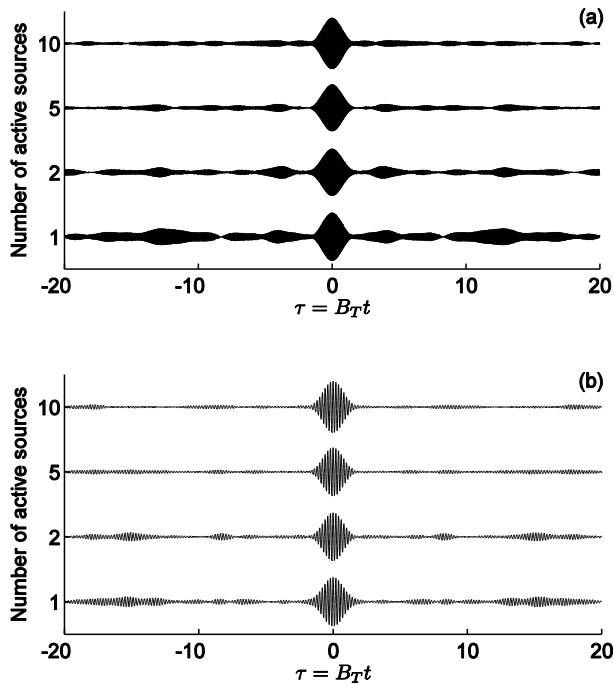


Figure 5 : A single realization of signals received for an increasing number of active sources, for $\nu_c = 0.7$ GHz and: (a) $B_T / \nu_c = 5\%$; (b) $B_T / \nu_c = 20\%$. The peak values attained by the signals are practically independent of the number of sources.

The different impact of pulse design and number of antennas is experimentally demonstrated in Figure 5, where signals received with different configurations are compared. These results confirm that increasing the number of antennas, even when weakly correlated ($\bar{\mu}_r \approx 10\%$), can be very ineffective, whereas bandwidth in a safe and usually cheaper solution.

While contrast is fundamental in order to have a proper transmission, the term accuracy also has another meaning: to have a stable transmission, i.e., to know beforehand the absolute level of the received signals, rather than just their relative value with respect to a random background. The derivation of (16) led to the conclusion that time-reversed transmissions generate signals (and fields) random in amplitude, behaving as Gaussian distributed random variables with standard deviations scaling as $\sqrt{B_c/B_T}$. This prediction was experimentally validated in [26], for target signals centered at 2 GHz and a varying bandwidth. Figure 6 compares empirical histograms with the theoretical probability density function of a standardized Gaussian random variable. Even in the case of $B_T = 2$ MHz, i.e., for $B_T/B_c \approx 4$, the probability distribution of the amplitude of the received signals is consistent with the theoretical one.

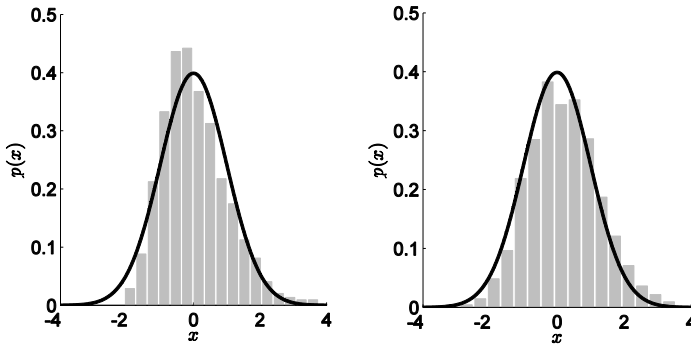


Figure 6 : Empirical and theoretical pdfs of the standardized variable $(\|y(t)\|_\infty - u)/\sqrt{u}$, with $u = \bar{W} B_T/B_c$, for $B_T = 2$ MHz (left) and 32 MHz (right). These results confirm the statistical convergence of the peak of time-reversed signals, as controlled by u . \bar{W} is the average value of the time-reversal transfer function $W(v)$ computed over B_T .

This agreement implies that given the maximum admissible variations in received signals, the minimum bandwidth B_T of the target signal can be chosen in a straightforward manner.

1.3.4 Polarization selectivity

Time reversal is usually demonstrated with scalar quantities. Having originated in acoustics, this is not surprising; but applications to electromagnetics have also been mainly limited to received signals, thus intrinsically scalar [19, 27, 28, 29, 30, 31, 32].

Still, time reversal can be used in case of vector fields are of interest. When done in diffusive media this takes on a particular significance and leads to another remarkable property: a single scalar signal can control the polarization of a vector field, just by changing its time evolution. This property was first demonstrated in [33].

In order to understand how a scalar excitation could control vector fields, let us consider the vector transfer function $\Phi(\nu)$ between a voltage $X(\nu)$ applied to the input port of an antenna and the electric field it generates at a given position within a diffusive medium, such that

$$\mathbf{E}(\mathbf{r}, \nu) = \Phi(\nu)X(\nu) \quad (27)$$

where the transfer function can be expanded into a (eventually infinite) summation of eigenmodes $\mathbf{e}_m(\mathbf{r}, \nu)$, i.e., solutions to the sourceless version of Helmholtz equation, as

$$\Phi(\nu) = \sum_m^M \gamma_m \mathbf{e}_m(\mathbf{r}, \nu) \quad (28)$$

with \mathbf{r} the position at which the field is sampled; the γ_m are modal coefficients expressing the rate of excitation and relative phase shift of the modes.

In disordered media, and particularly in diffusive media, fields are expected to be not only randomly distributed, but also randomly polarized, as recalled in Section 1.2, i.e.,

$$\langle \Phi \Phi^H \rangle \propto \mathbf{1} \quad (29)$$

with $\mathbf{1}$ the identity matrix and H the Hermitian transpose. Eq. (29) contains multiple statements: not only each polarization has the same average intensity, but also each couple of different polarizations are ideally uncorrelated. This property is expected for each frequency only across multiple random realizations.

In practice, the idea of having to generate a set of realizations in order to access an interesting property is a big turn off, making a potentially useful property more of theoretical observation.

Time-reversed signals work across the frequency axis and can be shown to make this property accessible and usable in practice. It has been observed in [34] that exciting a reverberation chamber at different frequencies is equivalent to generating a set of random realizations. In spite of the fact that this property evokes the idea of ergodicity, it would be incorrect to take it for granted. A better explanation of this property is to be sought in the statistical properties of resonant frequencies of large cavities, as studied in wave chaos theory [35]. We will leave this topic to the interested Reader and focus on this apparent ergodicity for our practical purposes.

In short, as the modes M in a medium excited over the bandwidth B_T of a target signal increases, the number of modes contributing to the overall field will also increase, averaging out their random contributions. If the random properties of these modes are assumed (as discussed above) to be identical when looking at different realizations or at different frequencies, the following asymptotic equivalence holds

$$\lim_{M \rightarrow \infty} \int_{B_T} d\nu \Phi(\nu) \Phi^H(\nu) \propto M \langle \Phi(\nu_c) \Phi^H(\nu_c) \rangle \quad (30)$$

This abstract-looking result is in fact of great practical utility. Let us now consider an excitation signal

$$X(\nu) = P(\nu) \Phi^H(\nu) \hat{\mathbf{p}} \quad (31)$$

where $P(\nu)$ is the Fourier spectrum of the target signal and $\hat{\mathbf{p}}$ is the polarization along which this signal should appear, as a field. In case the target signal is a pulse reaching its peak around $t = 0$, the resulting field reads

$$\mathbf{E}(\mathbf{r}, 0) = \int_{B_T} d\nu P(\nu) \boldsymbol{\Phi}(\nu) \boldsymbol{\Phi}^H(\nu) \hat{\mathbf{p}} \quad (32)$$

which, in case of an ideal diffusive medium, simplifies thanks to (29) and (30) into

$$\mathbf{E}(\mathbf{r}, 0) \simeq E_o \hat{\mathbf{p}} \quad (33)$$

where E_o is the root-mean-square intensity of any of the scalar components of $\boldsymbol{\Phi}(\nu)$, i.e., directly related to the energy density excited within the medium. The trick behind this result is the same already used to understand self-averaging in Section 1.3.1, i.e., taking advantage of the different frequency scales over which operate the medium transfer functions and the target spectrum.

Eq. (33) states that asymptotically time-reversed fields can exert a perfect control of their polarization, for any chosen target polarization $\hat{\mathbf{p}}$.

This theoretical prediction is proven correct in Figure 7, where the Cartesian field components generated by time-reversal excitations as in (31) are shown; three different choices for the final field polarization $\hat{\mathbf{p}}$ are considered. Random background fluctuations are still present, as shown in Section 1.3.2, so field polarizations can be controlled only when the target signal reaches its strongest intensity.

Figure 7 shows just one realization of time-reversed fields. Repeating these experiments over 50 positions distributed in a reverberation chamber led to the results shown in Figure 8 [36].

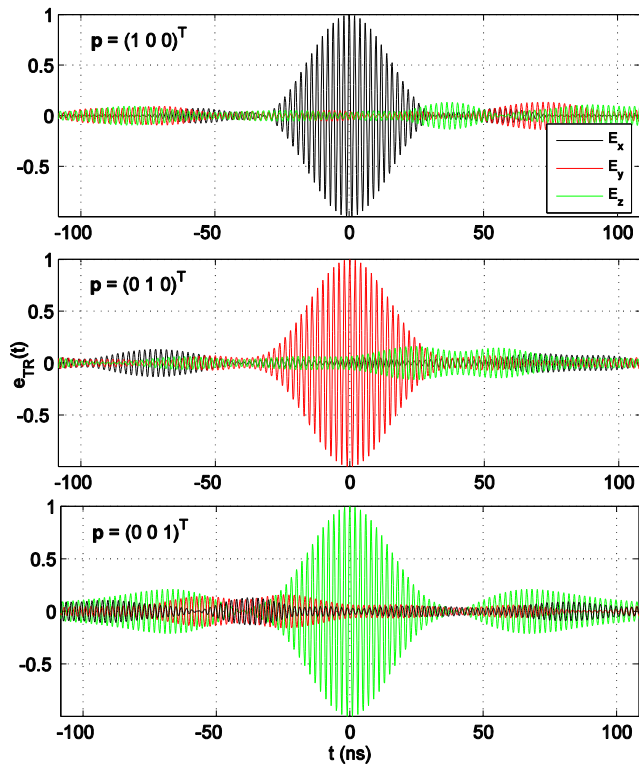


Figure 7 : Field components obtained from experimental results measured at one position, for Gaussian pulse at 1.5 GHz Each plot refers to weight vector \mathbf{p} corresponding to one Cartesian direction. Top to bottom, x, y, z components of fields are ideally the only excited when pulse attains peak value.

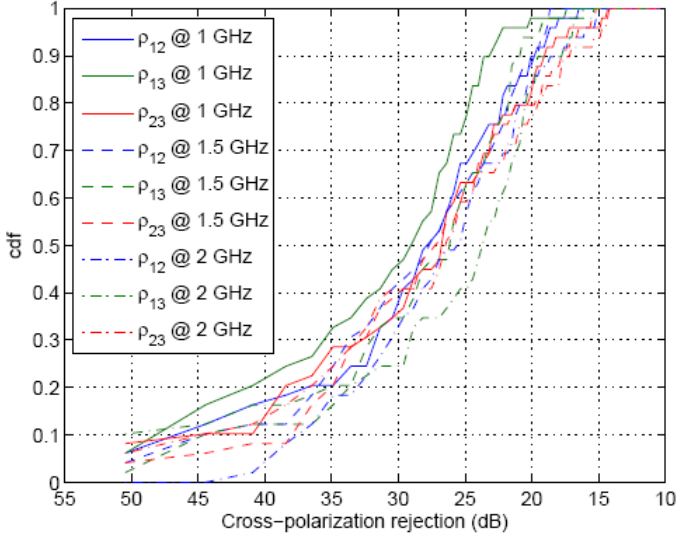


Figure 8 : Empirical probability distribution for cross-polarization rejections experimentally observed in time-reversed fields, generated to have a dominant linear polarization.

These results prove that in a diffusive medium, well-polarized fields can be generated even with antennas not intended for this purpose. Polarization rejections better than 25 dB were observed in half of all the cases tested; in 90 % of the experiments the rejection was close to 20 dB. A generic rejection is indicated as $\rho_{ij} = E_i/E_j$, with E_i one of the two cross-polarization components and E_j the co-polarization one.

These results laid the foundations for the generation of coherent wavefronts within reverberation chambers, presented in Section 1.4. Indeed, only when polarizations can be controlled a wavefront can be generated. Being able to do so with a single antenna bearing no specific features makes it possible to define novel applications for time reversal, but only when applied to diffusive media.

1.3.5 Conversion efficiency and power gain

The space-time compression operated by diffusive media excited with time-reversed excitation can be exploited in a further way. Suppose an input signal is applied to an

antenna used for exciting a reverberation chamber. After a transient, the energy injected is on average uniformly distributed over the entire volume of the chamber. A receiver would thus intercept at a given time only a small portion of this energy, which will meanwhile keep propagating *incoherently* throughout the volume of the chamber. If the receiver were an electric equipment tested within the chamber, then it would be submitted to a relatively weak electromagnetic stress, with respect to the total energy present inside the chamber.

In the case of time reversal, this picture can be partially subverted by having at least a portion of the energy converging (or focusing) *coherently* onto the equipment under test, at a given position and time. But at the same time, time-reversed signals generated in a reverberation chamber have an extremely low peak-to-average ratio, as shown in Figure 3(a) at page 11. In other words, for a given input energy, the peak power attained by the excitation signal can be a fraction of the signal that will be focusing within the chamber.

This idea was first suggested in [37] and can be formalized by introducing the notion of conversion efficiency, as the ratio between the peak instantaneous power observed by a receiver and the one of the input signal.

$$\eta_s = \eta[x_s(t)] = \frac{\|p_r(t)\|_\infty}{\|p_i(t)\|_\infty} \quad (34)$$

where the received power is defined with respect to an ideal sampler of the $\hat{\mathbf{q}}$ -aligned field component

$$p_r(t) = C_r[\mathbf{e}(t) \cdot \hat{\mathbf{q}}]^2 = C_r f^2(t) \hat{\mathbf{q}} \quad (35)$$

with C_r a constant modelling the antenna factor of the sampler, e.g., a probe. The definition of the input power refers to the excitation signal $x(t)$,

$$p_i(t) = C_i x^2(t) \quad (36)$$

The measured field $f(t)$ is related to the excitation signal by means of a transfer function $\Phi(\nu)$, such that $f(t) = F^{-1}\{\Phi(\nu)X(\nu)\}$, with F^{-1} the inverse Fourier transform and $X(\nu)$ the Fourier spectrum of $x(t)$.

The conversion efficiency can then be computed for a continuous-wave (CW) excitation of a reverberation chamber as,

$$\eta_{CW} = \frac{C_r}{C_i} W(v_c) \quad (37)$$

where $W(v) = |\Phi(v)|^2$ is the time-reversal transfer function introduced in Section 1.3.1.

Computing the same quantity for time-reversed excitations is trickier. In this case, $x_{TR}(t) = p(t) \star \phi(-t)$, where $p(t)$ is the target pulse meant to be reproduced at the probe position. One of the difficulties is to take into account the fact that the peak power of a time-reversed excitation is now a random quantity. This problem is addressed in [26] by introducing a multiplier K modelling how much $\phi(t)$ can exceed its root-mean-square envelope, corresponding to $\langle |\phi(t)|^2 \rangle = A_0^2 \exp(-2t/\tau)$, thus yielding

$$K^2 = \left\| |p_{i(t)}| \right\|_{\infty} / A_0^2 \quad (38)$$

The K factor, dubbed overshoot factor, is a random quantity; the interested Reader can find a derivation of its probability distribution in [26].

The main impact of the randomness of the time-reversed excitation is the impossibility to ensure a fixed peak power. As a result, for a given output field, the excitation required could vary, thus displaying a random efficiency. This is the opposite of what happens for the CW efficiency: in that case the input excitation is deterministic, and the output field is random. The main difference between the two cases is the probability distribution behind these quantities, which has a very different nature, as discussed in [26]; the dispersion is much higher for CW excitations.

The resulting efficiency is given by

$$\eta_{TR} = \frac{C_r B_T \kappa^2}{C_i B_c K^2} \bar{W}(v_c) \quad (39)$$

where the overbar stands for the average value computed over the bandwidth B_T of the target pulse. The shape factor κ^2 measures how pulse-like the target signal is, and is defined as

$$\kappa^2 = B_T \bar{P}^2 / E_p \leq 1 \quad (40)$$

where \bar{P} is the average of the spectrum of the target signal and E_p its mathematical energy.

Comparing (37) and (39) two differences come to mind. First the factor B_T/B_C in the time-reversal case can be expected to lead to much higher efficiencies; its physical origin is to be sought in the self-averaging mechanism offered by diffusive media, summarized in Section 1.3.1 and is the main reason for the improved efficiency of time-reversed excitations. It was already pointed out in Sections 1.3.1 and 1.3.3 as the main asset of time reversal in diffusive media.

Second, while the CW efficiency is based on a single realization of $W(\nu)$, thus wildly random, the time-reversal one is rather based on its average $\bar{W}(\nu_c)$, which can be made practically deterministic. We have already pointed at the fact that the overshoot factor in (39) is also random but it is actually much less dispersed than $W(\nu)$, which follows an exponential probability function, i.e., with a standard deviation equal to its average: a single realization as in (37) is therefore a risky bet. Hence the need for CW excitations for stirring solutions, in order to generate multiple independent realizations. To increase the chances of producing higher efficiencies.

Indeed, a more realistic definition of CW efficiency should take into account N runs at generating high fields from the same input signal, equivalent to throw a dice several times and keeping the best outcome. For instance, as in

$$\eta_{CW}^N = \max_{i \in [1, N]} \eta_{CW}^{(i)} \quad (41)$$

This extended definition is still badly dispersed, but the average of the CW efficiency can now be increased, though ineffectively, by increasing N .

In order to compare the two efficiencies their respective statistical modes are taken as good representations of typical values. The power gain

$$G_P^N = \frac{\text{Mo}[\eta_{TR}]}{\text{Mo}[\eta_{CW}^N]} \quad (42)$$

is now regarded as a potential gain in the conversion efficiency enabled by time-reversal excitations. The reason for calling it a power gain is to be understood by noticing that for a fixed output power, an increase in the conversion efficiency would correspond to a reduction in the input power needed.

It can be proven that (42) is well approximated by [26]

$$G_P^N = \frac{B_T}{B_c} \frac{\kappa^2}{\ln N} \left[a \ln^b(4 B_T/B_c) \right]^{-2} \quad (43)$$

with $a = 0.749, b = 0.678$. The power gain is now clearly dominated by the $B_T/B_c \ln N$ term, which exposes the inefficiency of the CW approach. Having N degrees of freedom (perfect stirring states) just increases the efficiency as their natural logarithm, while time-reversed excitations can take full advantage of B_T/B_c degrees of freedom. This difference is due to the collaborative nature of time reversal where the B_T/B_c degrees of freedom are coherently excited. This result was tested in [26] against experimental results, finding a good agreement with theory, as reported in Figure 9.

The differences in the efficiencies can be better grasped by imposing an equal typical performance for the two excitations, so that (43) can be converted into

$$N = \exp \left\{ \frac{B_T}{B_c} \left[a \ln^b(4 B_T/B_c) \right]^{-2} \right\} \quad (44)$$

for $\kappa = 1$. This last result estimates the typical number of stirring states needed for a CW excitation to compare favorably with time-reversal excitations, and is shown in Figure 10.

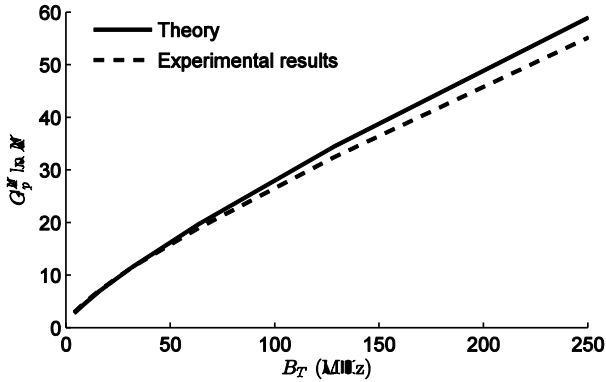


Figure 9 : Normalized gain $G_p^N \ln N$ as a function of B_T .

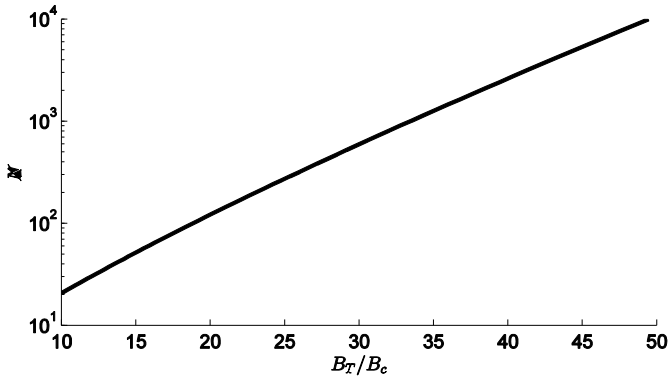


Figure 10 : Equivalent number of independent realizations required in a CW-driven reverberation chamber, in order to ensure the same typical efficiency as when time-reversal driven, as defined by (44).

Not only are time-reversed excitations more efficient than self-averaging, but also less statistically dispersed, since coherent excitation of the degrees of freedom is equivalent to a sample average. The central limit theorem applies in this case, implying a convergence to the average. Figure 11 shows the 95 % confidence intervals computed for the two excitation schemes normalized to their respective average values, as the number of available degrees of freedom is increased. The steady convergence of time-reversed excitations leads to fields characterized by amplitudes that can be practically considered as deterministic with a hundred degrees

of freedom, whereas CW excitations would still generate typical relative dispersions of about 100 %.

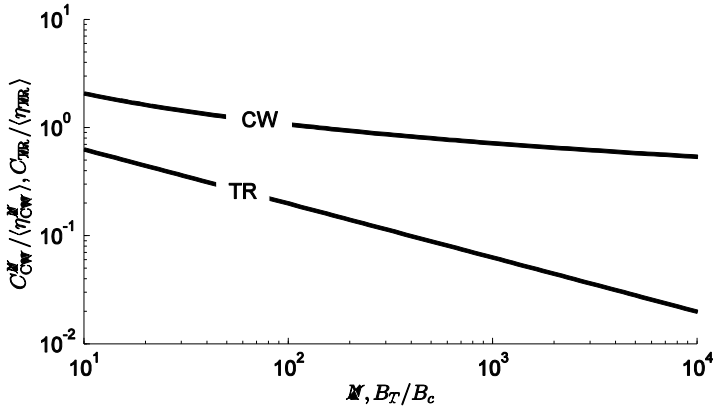


Figure 11 : Relative confidence intervals of the conversion efficiencies for a 95 % probability, as a function of the number of degrees of freedom.

These results point to the possible use of time-reversed excitations as a threefold solution: stronger fields, more predictable and in one shot, i.e., without repeating tests along stirring positions.

1.4 Time Reversal for the generation of wavefronts

So far time reversal has been applied to diffusive media in order to produce either an output signal at a receiving antenna or as a way of generating a field at a specific position. Both cases can be seen as a point-to-point transmission scheme.

This section rather explores the use of time reversal as a way of generating wavefronts within a diffusive medium. This possibility was first empirically demonstrated in a number of papers [38, 20, 39, 40], with the first demonstrations in acoustics. The question of how well a time-reversed wavefront is reproduced in a diffusive medium is first addressed from a theoretical point of view in Section 1.4.1, by introducing the time-reversal dyadic functions that relate the wavefront generated by means of time reversal within a given medium to the target wavefront expected to be generated.

The first phase usually taken for granted in time-reversal applications is argued in Section 1.4.2 to be a major obstacle in the development of test facilities based on time reversal. From these observations, a generalized approach to time reversal is presented in Section 1.4.3, where the first phase is avoided by directly synthesizing the excitations signals that would usually be expected to be recorded during the first phase.

A practical implementation of generalized time reversal is then discussed in Section 1.4.4, describing a robot prototype developed in CentraleSupélec. Experimental results obtained with it are shown and analyzed in Section 1.4.5, validating the possibility of designing test facilities based on time reversal principles.

1.4.1 Time-reversal dyadic function

With reference to Figure 12, consider a source of radiation occupying a region Ξ . Modelling it as a combination of electric and magnetic currents, respectively noted as $\mathbf{J}_e^s(\mathbf{r})$ and $\mathbf{J}_m^s(\mathbf{r})$, the electric field it produces can be written as

$$\mathbf{E}_{\text{wf}}(\mathbf{r}) = \int_{\Xi} d\mathbf{r}' \mathbf{G}_{ee}(\mathbf{r}, \mathbf{r}') \cdot \mathbf{J}_e^s(\mathbf{r}') + \int_{\Xi} d\mathbf{r}' \mathbf{G}_{em}(\mathbf{r}, \mathbf{r}') \cdot \mathbf{J}_m^s(\mathbf{r}') \quad (45)$$

where the integrals are computed over the volume of Ξ ; $\mathbf{G}_{ee}(\mathbf{r}, \mathbf{r}')$ and $\mathbf{G}_{em}(\mathbf{r}, \mathbf{r}')$ are the Green's functions of the propagation medium for the electric field generated by electric and magnetic currents, respectively. In order to derive the relationship between the wavefront generated by means of time reversal and that radiated by the original source, it is convenient to define an auxiliary surface Σ , chosen spherical of radius r_{Σ} , as in Figure 12; this surface can be in the near-field region of the source.

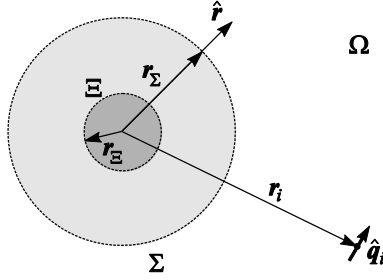


Figure 12 : Configuration for the application of Love's equivalence theorem.

Equivalent electric and magnetic currents are defined over the surface, representing the wavefront $\mathbf{E}_{wf}(\mathbf{r}, t)$ that would have been generated by a synthetic source contained in the volume bounded by the surface Σ . The dipole polarized along $\hat{\mathbf{q}}_i$ is a TRM antenna. These elements are embedded within a diffusive medium.

Sampling the electromagnetic field radiated by the source over Σ , equivalent electric and magnetic currents can be defined, as stated by the equivalence theorem [41]

$$\begin{aligned} \mathbf{J}_e(\mathbf{r}) &= -\zeta_o^{-1} \delta(r - r_\Sigma) \mathbf{1}_t \cdot \mathbf{E}_{wf}(\mathbf{r}) \\ \mathbf{J}_m(\mathbf{r}) &= \delta(r - r_\Sigma) \mathbf{E}_{wf}(\mathbf{r}) \times \hat{\mathbf{r}} \end{aligned} \quad (46)$$

where $\delta(\cdot)$ is the Dirac distribution, here used to represent sampling over the surface Σ ; ζ_o is the wave impedance of the background medium, e.g. air; $\mathbf{1}_t$ is the transverse identity dyad, which strips a vector of its radial component, leaving only the transversal components intact, here used in order to extract the tangential components of the electric field with respect to the surface Σ .

The field radiated by the source can now be written as

$$\mathbf{E}_{wf}(\mathbf{r}) = \int_{\Sigma} d\mathbf{r}' \mathbf{G}_{ee}(\mathbf{r}, \mathbf{r}') \cdot \mathbf{J}_e(\mathbf{r}') + \int_{\Sigma} d\mathbf{r}' \mathbf{G}_{em}(\mathbf{r}, \mathbf{r}') \cdot \mathbf{J}_m(\mathbf{r}') \quad (47)$$

where integrals are now taken over the surface Σ and involve the equivalent current distributions. If the TRM antenna in Figure 12 has an effective height $\mathbf{h}_e(\nu) = h_e(\nu) \hat{\mathbf{q}}$, eventually frequency dependent, the following vector transfer functions can be introduced

$$\begin{aligned} \mathbf{N}_e(\mathbf{r}) &= \mathbf{G}_{ee}(\mathbf{r}, \mathbf{r}') \cdot \hat{\mathbf{q}} \\ \mathbf{N}_m(\mathbf{r}) &= \mathbf{G}_{em}(\mathbf{r}, \mathbf{r}') \cdot \hat{\mathbf{q}} \end{aligned} \quad (48)$$

so that the signal received by the TRM antenna during the first phase reads

$$V(\nu) = C_1(\nu) \left[\int_{\Sigma} d\mathbf{r}' \mathbf{N}_e(\mathbf{r}') \cdot \mathbf{J}_e(\mathbf{r}') + \int_{\Sigma} d\mathbf{r}' \mathbf{N}_m(\mathbf{r}') \cdot \mathbf{J}_m(\mathbf{r}') \right] \quad (49)$$

with $C_1(\nu)$ a scalar taking into account all frequency-related effects, such as an eventual dispersion of the receiving antenna.

Injecting the phase-conjugated (or time-reversed) version of $V(\nu)$ into the antenna, i.e., $V_{\text{in}}(\nu) = V^*(\nu)$, the field thus generated is given by

$$\begin{aligned} \mathbf{E}_{TR}(\mathbf{r}) &= C_2(\nu) \left[\zeta_o^{-1} \int_{\Sigma} d\mathbf{r}' \mathbf{N}_e^*(\mathbf{r}') \mathbf{N}_e(\mathbf{r}) \cdot \mathbf{E}_{\text{wf}}^*(\mathbf{r}') - \right. \\ &\quad \left. \int_{\Sigma} d\mathbf{r}' \hat{\mathbf{r}} \times \mathbf{N}_m^*(\mathbf{r}') \mathbf{N}_e(\mathbf{r}) \cdot \mathbf{E}_{\text{wf}}^*(\mathbf{r}') \right] \end{aligned} \quad (50)$$

with $C_2(\nu)$ now also taking into account the frequency dependencies during the transmission phase.

Fields propagating through diffusive media can be treated as random variables, as discussed in Section 1.2, so that also $\mathbf{E}_{TR}(\mathbf{r}, \nu)$ should at first sight be regarded as random in nature. While technically correct, the randomness of $\mathbf{E}_{TR}(\mathbf{r}, \nu)$ can be practically ignored, as long as the wavefront $\mathbf{E}_{\text{wf}}(\mathbf{r}, \nu)$ covers a bandwidth at least two orders of magnitude wider than the coherence bandwidth of the medium. Under these conditions, the self-averaging property discussed in Section 1.3.1 is very effective, so that $\mathbf{E}_{\text{wf}}(\mathbf{r}, \nu) \simeq \langle \mathbf{E}_{\text{wf}}(\mathbf{r}, \nu) \rangle$, whence

$$\begin{aligned} \mathbf{E}_{TR}(\mathbf{r}) &\simeq C_2(\nu) \left[\zeta_o^{-1} \int_{\Sigma} d\mathbf{r}' \mathbf{T}_{ee}(\mathbf{r}, \mathbf{r}') \cdot \mathbf{E}_{\text{wf}}^*(\mathbf{r}') - \right. \\ &\quad \left. \int_{\Sigma} d\mathbf{r}' \mathbf{T}_{em}(\mathbf{r}, \mathbf{r}') \cdot \mathbf{E}_{\text{wf}}^*(\mathbf{r}') \right] \end{aligned} \quad (51)$$

where

$$\begin{aligned} \mathbf{T}_{ee}(\mathbf{r}, \mathbf{r}') &= \langle \mathbf{N}_e^*(\mathbf{r}') \mathbf{N}_e(\mathbf{r}) \rangle \\ \mathbf{T}_{em}(\mathbf{r}, \mathbf{r}') &= \langle \hat{\mathbf{r}} \times \mathbf{N}_m^*(\mathbf{r}') \mathbf{N}_e(\mathbf{r}) \rangle \end{aligned} \quad (52)$$

are dyadic functions dependent on the spatial correlation functions of the medium. The wavefront generated by means of time reversal can therefore be expressed as

$$\mathbf{E}_{TR}(\mathbf{r}) \simeq C_2(\nu) \int_{\Sigma} d\mathbf{r}' \mathbf{T}(\mathbf{r}, \mathbf{r}') \cdot \mathbf{E}_{wf}^*(\mathbf{r}') \quad (53)$$

with

$$\mathbf{T}(\mathbf{r}, \mathbf{r}') = \zeta_o^{-1} \mathbf{T}_{ee}(\mathbf{r}, \mathbf{r}') - \mathbf{T}_{em}(\mathbf{r}, \mathbf{r}') \quad (54)$$

the time-reversal dyadic function. Eq. (53) implies that wavefronts generated by means of time reversal are not mere replicas of an originally radiated wavefront $E_{wf}(\mathbf{r}, \nu)$, but rather appear to be subject to a point-spread function, $\mathbf{T}(\mathbf{r}, \mathbf{r}')$, in the shape of a dyadic function. This function may be expected to distort the original wavefront, both in its spatial evolution and polarization.

The previous results are completely general and can be applied to any medium, be it modelled as deterministic or random. For the special case of diffusive media, Section 1.2.2 recalled that field there generated have statistical properties that are invariant with respect to rotation and translation, but not polarization. These properties were used in the derivation presented in [42], deriving the time-reversal dyadic function for the case of diffusive media. Although the derivation is not discussed here, Figure 13 gives an example of the point-spread function, when sampled over a spherical surface. These data fundamentally show the distribution of the electric field that would be generated (on average) by time reversal, when attempting to reproduce a singular field distribution, i.e., a spatial pulse. Rather than reproducing the same distribution, Figure 13 shows that spatial resolution is limited and that depending on the polarization of the original field, that of the time-reversed wavefront can be critically affected.

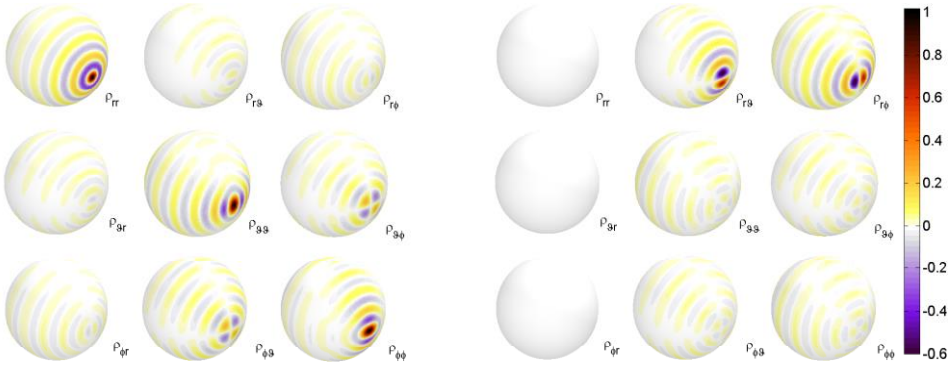


Figure 13 : Normalized dyadic function $\tilde{\boldsymbol{\rho}}(\mathbf{r}, \mathbf{r}', \nu)$ computed for $\mathbf{r} \in \Sigma$ and $\mathbf{r}' = r_{\Sigma} \hat{\mathbf{x}}$, with $r_{\Sigma} = 3\lambda$: (a) real and (b) imaginary parts. The 9 terms of the dyadic response are shown, matrix-wise, considering standard spherical unit vectors, following the order $\hat{\mathbf{r}}$, $\hat{\boldsymbol{\theta}}$ and $\hat{\boldsymbol{\phi}}$, defined with respect to a polar axis vertically oriented.

The point spread function basically appears for two reasons. First, time reversal operates on signals received by antenna typically electrically distant from the original source. Hence, mostly propagative components are sampled, while reactive ones, those associated to near-field characteristics, are lost. Second, focusing purely propagative components cannot reproduce the polarizations found in the reactive region of the source, as attested by the cross-terms in Figure 13. In other words, as long as only the propagative part of a wavefront is needed, this can be reproduced accurately by time reversal, even in a diffusive medium. Otherwise, solutions such as time-reversal sinks would be required [43], in order to reintroduce the lost reactive contributions.

1.4.2 The burden of a first radiating phase

Section 1.3 recalled how time-reversed signals are generated. In particular, it made clear that the very expression “Time Reversal” is in fact a truncated sentence, as it lacks an object. Indeed, it is not time that is reversed, but rather the time evolution of a wavefront; in particular, a wavefront first generated, e.g., by a source, like an antenna. Only after a TRM antenna has recorded the signature of the wavefront and

the distortion introduced by the propagation medium time reversal can operate its magic.

Figure 14 summarizes the two existing approaches used in time reversal in open media. The first method corresponds to what has just been recalled: a source of radiation is activated generating a diverging wavefront; after recording by the TRM antennas, the propagative part of the wavefront can be generated, this time as a wavefront converging back to its origin.

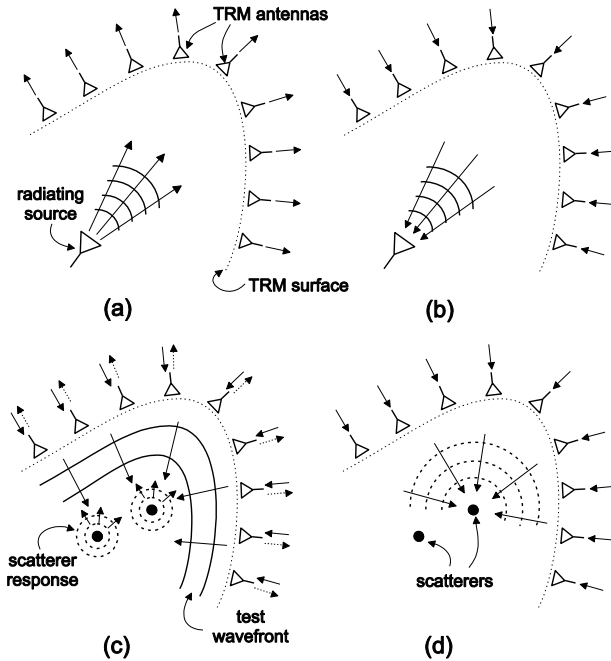


Figure 14 : A schematic representation of the two main time reversal techniques currently available: (a)-(b) time reversal of a radiating source; (c)-(d) selecting focusing over a point scatterer by means of the DORT approach.

While impressive in its effectiveness, this approach has a clear drawback: it is not possible to generate any wavefront on command, but only to reproduce what has been generated first by a source of radiation. Any application of time reversal aiming at generating focusing wavefronts in complex media are therefore hampered by the need: 1) to have an appropriate source of wavefronts that would then be time reversed; 2) to repeat this first phase of radiation before being capable of generating

the actual wavefront of interest, the focusing one. Imaging the case of a set of wavefronts to be generated, with different features, e.g., direction of arrival, directivity: an equivalent set of sources with different orientations will need to be available (and characterized). Such a cumbersome procedure goes against the very idea of a test facility, which is expected to be capable of generating test wavefronts straight away.

Suppose now the case of a passive piece of equipment, to be submitted to an impinging focusing wavefront. Following the above description, the diverging version of the wavefront will need to be generated, but by what source? The equipment under test is passive. Should an antenna, acting as an external source, be added over the position where the focusing wavefront will converge? But how to ensure that the field radiated by the antenna would not be modified by the boundary conditions imposed by the equipment?

A solution to this problem comes with the second configuration described in Figure 14. In this case, rather than time-reversing the wavefront radiated by a source, it is rather the wavefront scattered by the equipment that is focused back at its origin. This idea gave way to the DORT (Décomposition de l'Opérateur de Retournement Temporel) method [44, 45], where an object under test is submitted to a wavefront sounding it. The field thus scattered is recorded, post-processed through an eigenanalysis in order to define wavefronts that will focus over the brightest scattering points. Despite providing a solution to extend time reversal to the case of passive equipments, wavefronts thus generated are totally dependent on the equipment itself; necessarily only wavefronts corresponding to the equipment scattering can be reproduced. Moreover, the first phase is still there.

The rest of this section presents a solution capable of generating time-reversed wavefronts without involving any initial source. The method, denoted as generalized time reversal, or GTR, is first theoretically derived; requirements and limitations are then discussed; experimental results showing its ability to generate arbitrary wavefronts in a reverberation chamber are finally shown.

1.4.3 Direct wavefront synthesis

The derivation of the time-reversal dyadic function comes with an important by-product. Eq. (49), can be restated as

$$V(v) = C_1(v) \int_{\Sigma} d\mathbf{r}' N_{\text{eq}}(\mathbf{r}') \cdot \mathbf{E}_{\text{wf}}(\mathbf{r}') \quad (55)$$

where

$$\mathbf{N}_{\text{eq}}(\mathbf{r}) = -\zeta_o^{-1} \mathbf{N}_e(\mathbf{r}) + \hat{\mathbf{r}} \times \mathbf{N}_m(\mathbf{r}) \quad (56)$$

Eq. (55) now states that the voltage that would be received in presence of a source can actually be computed, as soon as the medium Green's function between the TRM antenna and the surface Σ are known, and converted into the function $N_{\text{eq}}(\mathbf{r})$.

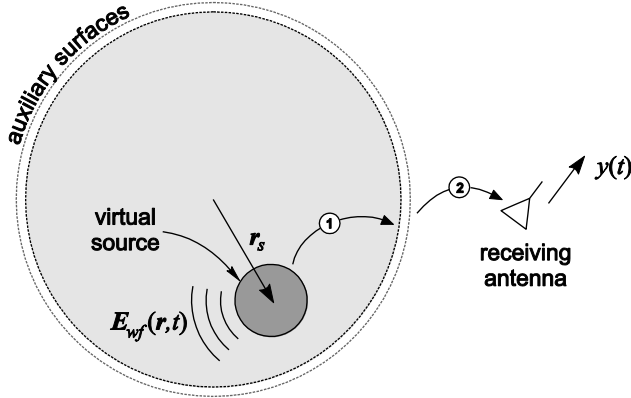


Figure 15 : Relevant quantities in the derivation of direct synthesis of excitation signals with GTR. The auxiliary surfaces are shown to act as an interface between the virtual source radiation (1) and its propagation through the medium (2).

The physical meaning of (55) is schematically represented in Figure 15, where the surface Σ acts as an interface between the field radiated by a source (step 1) and the TRM antenna (step 2). By performing step 1 offline, e.g., by using a closed-form expression for the field radiated by a source, or a numerical model of the source, (56) yields the received voltage. In the end, this process is equivalent to a virtual first phase, where sources of any kind are available. That said, it should be clear that the quality of time-reversed wavefronts strongly depends on their space and time evolution. A discussion about this point is presented in Section 1.4.5.

This result has practical implications, since it has the potential of bypassing the need for a first phase in time-reversal applications; the wavefront that would be generated by any source, could be time-reversed just by describing the field distribution it would generate over Σ . Since the entire procedure represents the propagation through the medium up to the TRM antenna, only propagative contributions will survive. For this reason, even if Σ were in the near-field region of the virtual source, only its propagative components need to be sampled over Σ . Therefore, the far-field radiation of the virtual source is sufficient, which is also simpler to compute than a full description of radiation valid also in the near-field region.

Direct synthesis is not the only advantage of this procedure. As discussed in Section 1.3.3, a single antenna can be good enough in a diffusive medium. Now, with direct synthesis, this antenna takes the central stage, as it becomes a wavefront synthesizer. A single antenna can thus potentially generate any wavefront just by acting on the signals applied to it. This procedure can be enacted in real time, as long as the Green's functions are measured and stored. Sequences of wavefronts can therefore be generated, e.g., in order to image systems under test, as discussed in Section 1.4.6.

The price to pay is now the need to know Green's functions over this same surface. This is a delicate task, since in the case of a diffusive medium they are unpredictable. On the one hand, numerical simulations are an unlikely solution, since they would be too sensitive to tolerances in boundary conditions; even it is was not the case, they would require a precise description of the medium, the materials involved and their geometry. Moreover, the reverberant nature of diffusive media imply long time evolutions, thus necessarily long simulation times. On the other hand, measuring Green's functions in a diffusive medium is not necessarily a simpler task: the medium sensitivity to any boundary modifications (e.g., antennas moving, metallic parts introduced, etc.) means that electromagnetic probes would need to be very weakly perturbative in order not to alter the medium. On top of this problem, field probes would have to be moved along Σ : certainly not by hand, since potentially thousands of positions would be needed. A solution to this problem is described in Section 1.4.4, based on an automatic experimental characterization of a diffusive medium.

1.4.4 Implementating GTR

In order to translate the idea of virtual sources from theory to practice, a number of issues need to be addressed. The most important is certainly to decide what kind of diffusive media should be used. At the beginning of this chapter we stressed how common are diffusive media; why then bother to pick one? Given a set of media sharing the same statistical properties (Section 1.2.2), a sensible criterion would be to compare their energy efficiencies. As a matter of fact, if GTR were used for the conversion of signals into wavefronts, and these wavefronts were meant for the radiative testing of a device or system, it is natural to prefer a medium that would generate the strongest possible fields for the same peak input power (Section 1.3.5). This preference takes its full sense when thinking of tests on non-linear devices, or in general in the case of devices with a threshold behavior: if an impinging field strong enough makes a device switch from an acceptable behavior to one where its basic workings is no longer ensured, it is important to have the ability to reach and test this region in the response of the device under test.

The most energy-efficient diffusive medium is the reverberation chamber, thanks to its reflective boundaries, defining a closed space where waves propagate through multiple scattering events. Low dissipation over these boundaries and an even lower rate of energy leakage make reverberation chambers the natural choice to implement GTR.

But the advantages of reverberation chambers come with drawbacks: featuring long time constants, due to the long number of times waves propagate through them before losing a substantial fraction of their energy, they are inevitably very sensitive to any modification along their propagation paths. Displaced boundaries, unless very weakly scattering, can have a dramatic impact on the transfer functions of a reverberation chamber. Modifications like these are an issue only in one case: if a transfer function is measured before (nominal case) and after the chamber is modified. If the nominal response were used for the prediction of the actual chamber response, its inaccuracy could make it useless. This is the second issue that needs to be solved: how to measure Green's functions in a medium that is so sensitive to modifications?

The solution comes in several steps. First, rather than applying elementary sources over Σ and measuring received voltages at the TRM antenna, the reciprocity of the medium can be assumed and exploited, by turning the approach upside-down: the TRM antenna is excited and the field it generates over Σ is now sampled by probes. The main difference in these two opposed scenarios is that the TRM antenna is already present, and thus does not alter the medium, as opposed to the case where sources would be placed over Σ . Moreover, very weakly scattering probes are available off the shelf, whereas elementary sources are more of a fiction. It goes without saying that these probes need to be phase sensitive. Manufacturers producing this kind of probes are Enprobe, Kapteos, Seikoh-Giken; this list is not exhaustive.

If electric- and magnetic-field probes are available, then (55) can be directly implemented. But in practice magnetic-field probes are less sensitive, and could have issues trying to properly measure the magnetic field generated by low-power sources, e.g., by a vector network analyzer. In such scenarios it is therefore necessary to modify (56) in order to have only Green's electric-electric function appearing. Demonstrating the feasibility of this idea is not trivial; the interested reader is invited to refer to [46] for a detailed discussion.

In the context of this chapter, we will stick to an intuitive explanation. Suppose to add to Σ another surface, concentric to it but with a radius larger by an amount ΔR . The two surfaces are now referred to as Σ_l , $l \in [1,2]$. The electromagnetic field radiated by the virtual source is sampled over these two auxiliary surfaces, yielding two sets of equivalent electric current distributions. If two points over the auxiliary surfaces are chosen to be along the same radial direction from the surfaces center, the two current elements thus selected can be regarded as forming a two-element end-fire array. In this respect, weights can be applied to them, in order to maximize the ratio between the outward and inward radiation. This idea can be formalized as done in [46], and shown to lead to

$$\mathbf{N}_{\text{eq}}(\mathbf{r}) = -\zeta_o^{-1} \sum_{l=1}^2 A_l \mathbf{N}_{e,l}(\mathbf{r}) \quad (57)$$

as a replacement to (56), with $\mathbf{N}_{e,l}(\mathbf{r})$ the electric field generated by the TRM antenna, as sampled over the surface Σ_l , and

$$A_1 = -\frac{\exp(-2jk\Delta R)}{1 - \exp(-2jk\Delta R)} \quad (58)$$

$$A_2 = -A_1 \exp(2jk\Delta R)$$

the weights applied to each layer of current.

Equipped with this updated formulation, the last remaining obstacle is the need to scan each auxiliary surface automatically. A solution has been presented in [47], based on a dielectric field scanner. The hardest problem in defining an automatic solution is to avoid modifying the propagation medium as a probe is moved over the surfaces. Clearly, it is not much the probe to blame, but rather the inevitable mechanical support meant to move it. Standard solutions based on metallic structures covered by absorbers are clearly not fit for the task, since they would maximally modify the behavior of a reverberation chamber.

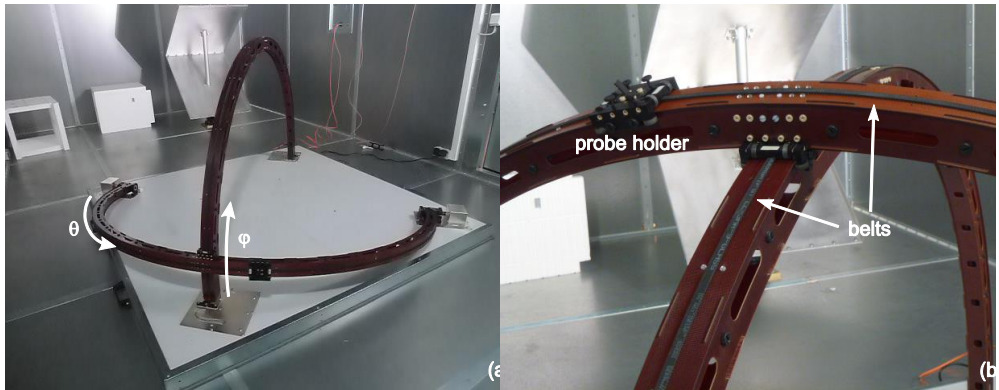


Figure 16 : The dielectric robot (a) with the two dielectric arms and its metallic platform hosting the motors and a close-up (b) of the arms crossing, showing the belts and probe holder.

Figure 16 shows two pictures of the robot developed in CentraleSupélec for this purpose. It is made of strands of fiber glass held together by a polymeric matrix. The two semicircular structures are hollow, 4 cm wide, with a thickness of 1 mm. They have sufficient rigidity as to ensure a precision of the end position of the probe within 1 mm. Two arms are used, one fixed, along φ , the other mobile, along ϑ .

The reason for choosing two structures rather than just one is to be found in the limited rigidity, or better Young's elastic modulus, of plastic materials, though it is remarkably high with respect to similar materials. The arch along the φ direction dramatically helps in reducing the deflection in the mobile arch, introducing a fixed support halfway along the mobile arch. Moreover, the fixed arch also offers a simple solution to the problem of putting in motion the mobile arch: directly applying a torque to the ends of the mobile arch is not an option, as it would require overlarge ends to stand the intense strain forces. It is rather simpler and more effective to have the mobile arch pushed and pulled by its middle point, where the two arms meet. A polymeric belt is used to this effect, as visible in Figure 16(b). A similar solution is used to move a probe holder guided along the mobile arch.

An experimental analysis of the perturbation introduced by this structure has shown that for an empty chamber the field scanner is practically invisible up to 1 GHz and start having a substantial impact on transfer functions (and thus Green's functions) above 3 GHz. As discussed earlier, if the number of times waves travel across the chamber were reduced, the perturbation would be better controlled. In practice, this amounts to increase dissipation, e.g., by introducing absorbers within the chamber. As discussed in [47], a single absorber pan would lead to an almost invisible scanner up to 3 GHz.

1.4.5 Retrieving free-space conditions: experimental results

The ideas introduced so far are here tested against experimental results. The main goal is to image the wavefronts generated with GTR, using the dielectric field scanner described in the previous section; theoretical predictions of wavefronts propagating in free-space conditions will serve as references in order to assess the accuracy of GTR.

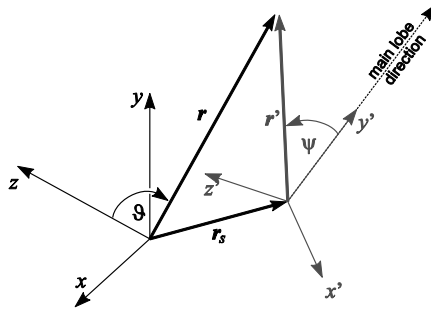


Figure 17 : Global and local reference frames for the computation of the vector field distribution at \mathbf{r} , radiated by a source centered over \mathbf{r}_s .

With reference to Figure 17, all wavefronts are chosen to share the same structure

$$\mathbf{E}_{wf}(\mathbf{r}, \nu) = \hat{\boldsymbol{\phi}} G(\mathbf{r} - \mathbf{r}_s, \nu) \exp(-\psi^2 / 2\psi_s^2) P(\nu) \quad (59)$$

where $G(\mathbf{r}, \nu)$ is the scalar Green's function for free-space propagation, \mathbf{r}_s is the position of the virtual source, ψ_s controls the angular divergence of the wavefront. The time-evolution of the wavefront, which is usually expected to follow a short pulse in applications of time reversal, is described by the Fourier spectrum $P(\nu)$, defined as

$$P(\nu) = \exp[-(\nu - \nu_c)^2 / 2\nu_s^2] \quad (60)$$

with ν_c the central frequency of the pulse and B_e its equivalent bandwidth.

In (59), the polarization of the wavefront is set by default along $\hat{\boldsymbol{\phi}}$, while the wavefront has a maximum of radiation along the y axis, where ψ approaches zero. In fact, this description refers to the local reference frame marked by primed quantities in Figure 17. In a general way, the wavefronts associated to (59) will be defined by local parameters, e.g., B_e, ν_c, ψ_s , and global ones, which describe how the local frame is oriented with respect to the global one. In this way, the main direction of propagation of the wavefronts can be changed, together with its co-polarization, by simply introducing a sequence of elementary rotations with respect to the global frame axis.

Eq. (59) is well-suited to describe the field radiated by the virtual source, but it cannot be used directly to compute the space-time evolution of the refocusing wavefront, which is expected to be generated by GTR thanks to (55) together with (56) or (57). In order to predict the refocused field distribution, the simplest option is probably to consider the far-field radiation pattern of the virtual source, e.g., by letting $\mathbf{r} = R\hat{\mathbf{k}}$, $R \rightarrow \infty$, along a generic direction $\hat{\mathbf{k}}$, an operation which corresponds to obtaining the plane-wave spectrum of the radiated field [23, 48]. It is then straightforward to compute the refocused field distribution, by phase-conjugating (i.e., time-reversing) the plane-wave spectrum

$$\mathbf{E}_{GTR}(\mathbf{r}, t) = \int d\nu e^{j2\pi\nu t} \int d\hat{\mathbf{k}} \mathbf{E}_{wf}^*(R\hat{\mathbf{k}}, \nu) e^{jk_o\hat{\mathbf{k}}\cdot\mathbf{r}} \quad (61)$$

It is worth recalling that while the field scanner described in Section 1.4.4 can only measure the transfer functions between the TRM antenna and the auxiliary surfaces $\{\Sigma_l\}$. While sufficient for the synthesis of the excitation signals, these data are of limited importance in the validation of GTR. This conclusion can be understood in light of the existence of a fluctuation background in time-reversal applications in diffusive media (see Section 1.3.2); only where wavefronts focus they can be stronger than the background. Unless a wavefront is made to focus close to the auxiliary surfaces, its intensity will practically be negligible with respect to the fluctuations. A validation of GTR must necessarily be sought around the focusing region.

Figure 18 shows the planar region that was manually scanned with an electric-field probe, while exciting the TRM antenna, in the same way as the scanner did over the hemispherical surface. The fixed arm of the scanner is shown for reference.

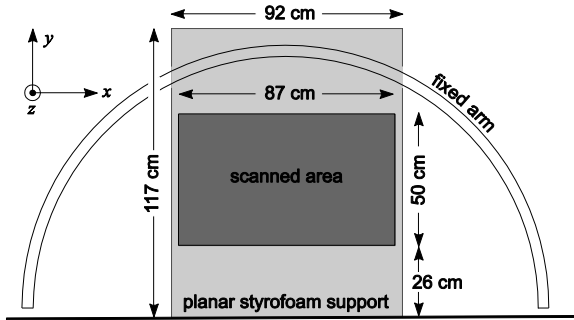


Figure 18 : Layout of the scanned planar area, as part of the xy plane of the global reference frame in Figure 17.

Calling these transfer functions $\mathbf{\Pi}(\mathbf{r}, \nu)$, the field generated by GTR can now be computed as

$$\mathbf{E}(\mathbf{r}, t) = \int d\nu \mathbf{\Pi}(\mathbf{r}, \nu) V^*(\nu) e^{j2\pi\nu t} \quad (62)$$

where $V^*(\nu)$ is the phase-conjugated version of (55). The field distributions over the planar region are computed from frequency-domain data, since otherwise the measurements would have had to be measured for each wavefront generated. Since the planar region is manually scanned, a time-domain approach would have been too time-consuming.

The results shown below refer to $\psi_s = 40$ degrees and $B_e = 0.5$ GHz, i.e., a strongly focusing wavefront, confined both in time and space. The theoretical and experimental distributions for a wavefront focusing at the center of the planar region are shown in Figure 19, for the two Cartesian field components lying on the plane. Only the instant $t = 0$ is shown, i.e., the time of focusing. The two distributions closely agree, and each scalar component of the electric field is well reproduced, as could have been expected from Section 1.3.4.

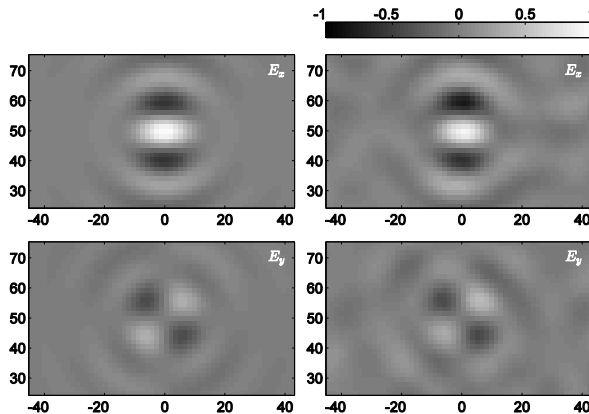


Figure 19 : Distributions of the horizontal (E_x) and vertical (E_y) field components expected (left column) and measured (right column) at $t = 0$ ns.

Restraining to the main polarization component, i.e., E_x , the time evolution of the GTR-generated wavefront in Figure 20 can be compared to the theoretical one in

Figure 21, from -5 ns up to 3 ns. These results show the instants during which the coherent energy starts to gather around the focus at -1.5 ns, building up the focal peak occurring around 0 ns.

The two sets of results agree very closely, confirming that a diffusive medium can indeed generate coherent wavefronts, and that GTR can do it without any original source later time reversed.

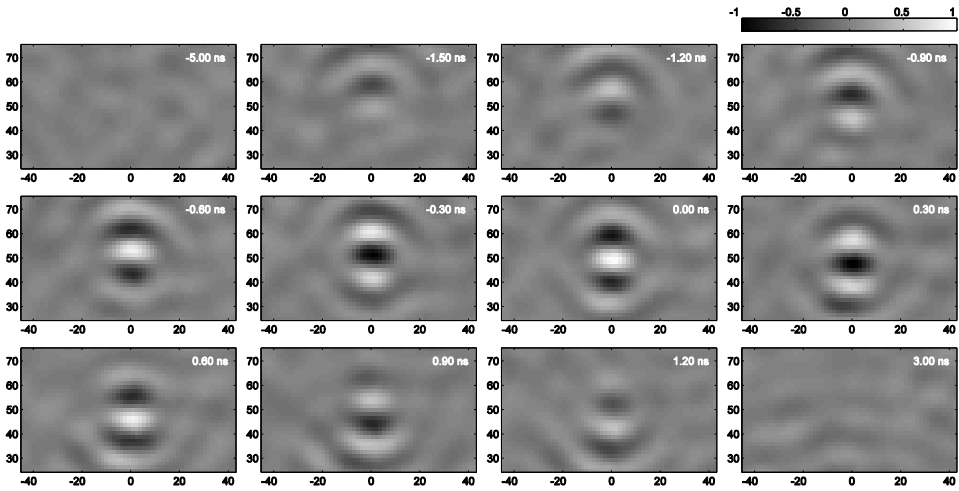


Figure 20 : Experimental distributions of the horizontal field component E_x expected over the region shown in Figure 18, for $\psi_s = 40$ degrees, $B_e = 500$ MHz.

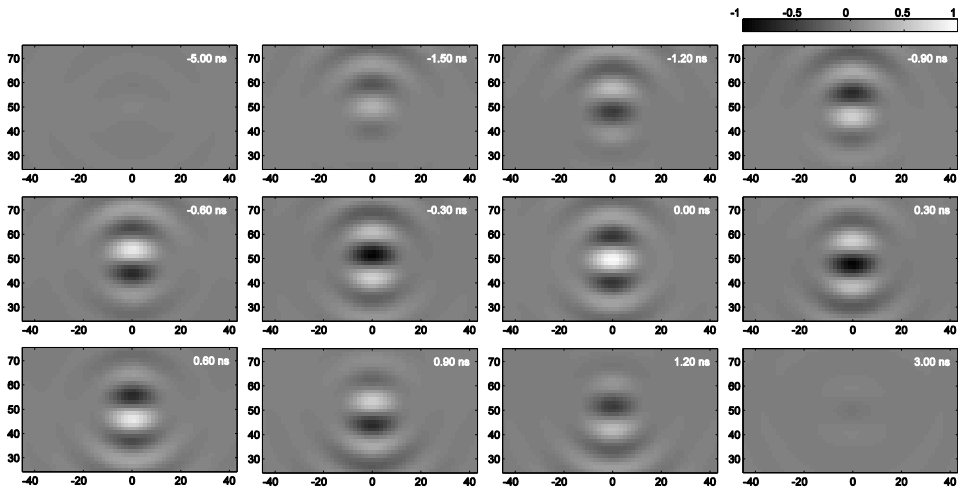


Figure 21 : Theoretical distributions of the horizontal field component E_x expected over the region shown in Figure 18, for $\psi_s = 40$ degrees, $B_e = 500$ MHz.

Two instants are perhaps even more revealing. The first we focus on occurs at 3 ns. At this time the coherent wavefront we wanted to generate has finished, as can be seen in Figure 21. But in Figure 20 it looks like a coherent wave is still propagating. The direction of curvature of the wavefront suggests that its phase center is now well below the imaged region, and the large curvature radius implies that the phase center should be looked for below the floor. In fact, at 3 ns the coherent wavefront has already reached the floor and reversed its direction of propagation after being reflected by the metallic floor. The phase center is therefore about 50 cm below the floor. This observation is very important, since it implies that the wavefront generated with GTR is not an illusion existing only for a short period of time, but it is a wavefront that is really propagating through the medium. Once coherent energy has been shaped into the wavefront, it is subject to the boundary conditions of the medium, and thus its reflections and scatterings can be observed, as long as its intensity is well above that of the background fluctuations.

The second instant of interest occurs at -5 ns, when the wavefront is still outside the imaged region, as confirmed by Figure 21. Looking at Figure 20, the field is not negligible, and closely looks like the speckle distributions discussed in Section 1.3.2.

This same kind of distribution, in particular its average intensity, can be observed in the background through all the time-domain results. As already pointed out in Section 1.3.2, these fluctuations are intrinsically caused by the properties of diffusive media, and therefore cannot be removed.

The problem should rather be looked the other way around, i.e., by looking for ways of having the coherent part of the wavefront standing out strongly enough to make background fluctuations negligible. It was recalled in Section 1.3.3 that the ratio between coherent and incoherent energies is fixed by the medium statistics. Hence, for a given background intensity, a coherent wavefront can stand out only when its energy is found within a region as compact as possible. In this case, even a small coherent energy can produce high local peaks of energy density, i.e., a peak in the electromagnetic field.

Only two options are thus available, either to focus energy in space or in time. In the first case, the plane-wave spectrum of the virtual source needs to cover the broadest spectrum of directions, in order to produce a small focal spot. As well-known from optical diffraction theory [22], this approach has its own limits, in the sense that the focal region cannot be made smaller than about half a wavelength; here the central frequency should be used for computing the wavelength. Moreover, increasing the divergence of the field radiated by the virtual source is not always possible, since it also impacts the way a wavefront excites an equipment under test, being richer or poorer in directions of arrival.

The second option available is to increase the bandwidth of the wavefront, in order to produce pulsed excitations. This approach has a limited impact on the shape of the focal spot, but again, it is not always viable, as it affects the response of an equipment under test. Examples of the way these two approaches affect the accuracy (and contrast) of GTR-generated wavefronts are shown in Figure 22.

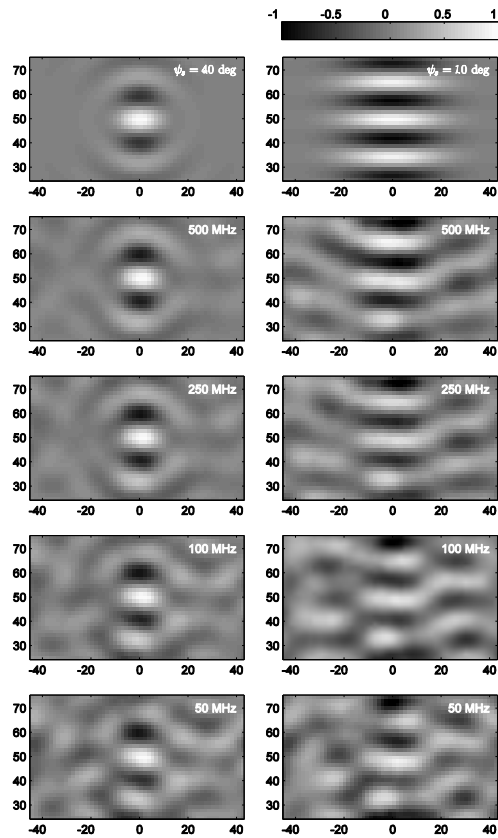


Figure 22: Comparison between the field distributions obtain for two Gaussian beams, with $B_e = 500$ MHz, for $\psi_s = 40$ degrees (left column) and $\psi_s = 10$ degrees (right column), as the equivalent bandwidth B_e changes. Notice how the focal region is hardly affected for $\psi_s = 40$ degrees, even for a relatively narrow bandwidth, as opposed to the case for $\psi_s = 10$ degrees.

The results shown so far have been obtained with a single focal position and direction of arrival of the wavefront. Test facilities involving radiated fields are based on the idea that independently from the position of the source and its orientation, the wavefronts are all identical apart for rotations and translations. The invariance of the wavefronts can also be expected for GTR, since diffusive media are characterized by spatial stationarity (translation invariance) and isotropy (rotational symmetry) of their statistical properties, as argued in Section 1.1. Experimental validation of these

predictions can be obtained very easily with GTR, as one just needs to change the description of the virtual source. First, spatial translations are considered. Figure 23 shows the field distribution generated at 0 ns by GTR, when the same virtual source is moved horizontally shifted. The reproducibility is excellent, with no visible differences apart from the background fluctuations.

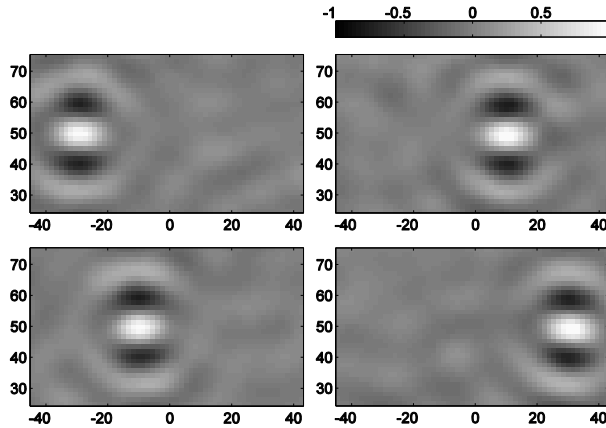


Figure 23 : Measured field distributions of E_x , for $\psi_s = 40$ degrees, $B_e = 500$ MHz and $t = 0$ ns, as the position of their focus is displaced horizontally, by 20 cm steps.

In a similar way, rotational invariance was tested, by acting on the orientation of the local reference frame in Figure 17. Figure 24 shows the result of the rotations; since with rotations the dominant role of a single Cartesian field component is lost, results are now shown as vector fields, together with a color-coded representation of the field norm. Again, the focal spot is very well preserved through the rotations.

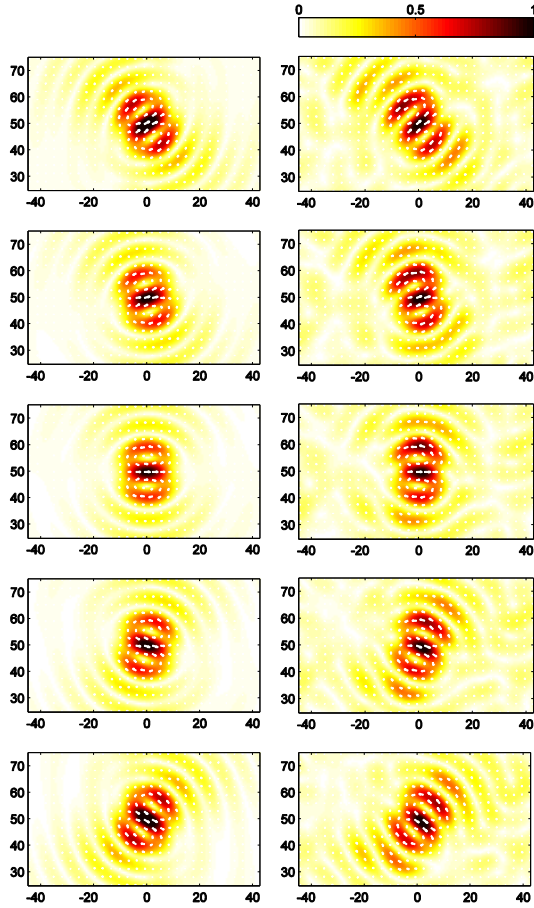


Figure 24 : Vector field distributions (theoretical on the left and measured on the right), for $\psi_s = 40$ degrees, $B_e = 500$ MHz, at 0 ns, for wavefronts impinging along a direction of arrival $\hat{\mathbf{r}}_{\text{inc}} \in xy$, rotated by 20 degree steps, from -40 to 40 degrees with respect to the y axis.

1.4.6 An original application: imaging apertures in a metallic shield

Wavefronts generated with GTR can be used as excitations for any test involving electromagnetic radiations. The advantages of using GTR in diffusive media have already been stated, but two of them have a special importance, in our opinion: the ability to generate focusing wavefronts and to do it on the go. Focusing wavefronts are important since they rhyme with spatial resolution, i.e., applying electromagnetic stress only to a small region of space, as opposed to diverging wavefronts.

One example of an application where these two properties are useful is the search for apertures in a metallic shield. Wavefronts generated by standard facilities, such as in anechoic chambers, have no resolution power, since they are supposed to locally mimic plane waves. As a result, when they impinging on an equipment under test, they excite a large portion of its surface at the same time: if one or more apertures are excited at the same time, it is hardly possible to distinguish their respective contributions.

GTR hands a nice solution to this problem. Focusing wavefronts can be defined and generated as a testing tool to apply stress only to a portion of the equipment surface. If an aperture exists at the position where the wavefront impacts, energy is transmitted inside the shield; it can then be measured by means either of a probe inserted for this purpose, or by monitoring voltages or currents along the circuits hosted inside the shield. If the wavefront is then translated to scan the entire shield surface, step by step, an image can be produced, translating how much energy is coupled through a given region of the shield.

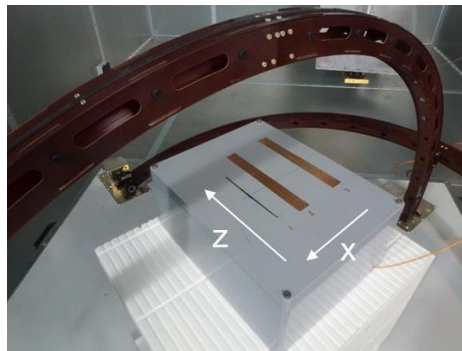


Figure 25 : Slotted metallic box imaged by scanning its top surface with focusing wavefronts.

This idea was tested on the metallic shield in Figure 25. Several slots were cut through its top surface, but only one at the time was left open, with the others covered with copper foil tape, in order to study the different responses of the shield when a slot has a different position. In the rest of this section only the configuration shown in Figure 25 is discussed.

The shield was tested by having wavefronts focusing on specific positions over the top surface of the shield, with their main lobe oriented orthogonally to it. The orientation of propagation of the wavefronts was kept unchanged through all the tests, even though it can easily be changed. Two polarizations were used, in order to have the focal spot of the impinging wavefront polarized either along x or z . The central frequency was chosen to be 2 GHz, as it ensures a spatial resolution below 10 cm, according to the diffraction limit. Several bandwidths were considered, in order to show how this parameter impacts the images.

Focal spots are meant to scan the plane tangent to the shield top surface, by changing the position of the associated virtual source. In order to ensure that the wavefront testing the shield at each position is seen as descending down onto the shield, it is fundamental that the wavefront corresponds to a plane-wave spectrum different from zero only for these downward directions.

The effects that these wavefronts have on the shield were measured by introducing an electric-field probe through one of the lateral surfaces of the shield, as can be seen in Figure 25. The peak intensity of the signals received by the probe were recorded for each position scanned, thus forming an image of the coupling through the shield surface.

Figure 26 shows the results of this operation. The coupling strength, measured by the peak of the signals received by the internal probe, is color-coded in order to ease the interpretation of the results. Starting with the first column (1 GHz equivalent bandwidth), the results show a coupling around the position of the only open slot, by far stronger when submitting the shield to x -polarized fields, than with z -polarized fields. This is consistent with the polarization filtering imposed by a thin slot, acting as an under-cut waveguide for z -polarized fields. The region of strong coupling appears smeared outside the slot perimeter, as is inevitable due to the finite dimensions of the focal spots used during the scans: hence, even when hitting the shield about a quarter of wavelength away from the slot, a substantial portion of

energy is still applied over the slot. The random distributions appearing in the background when the coupling is at its lowest are due again to background fluctuations generated by time-reversed signals within diffusive media, which is always present and thus couples in any case to the interior of the shield.

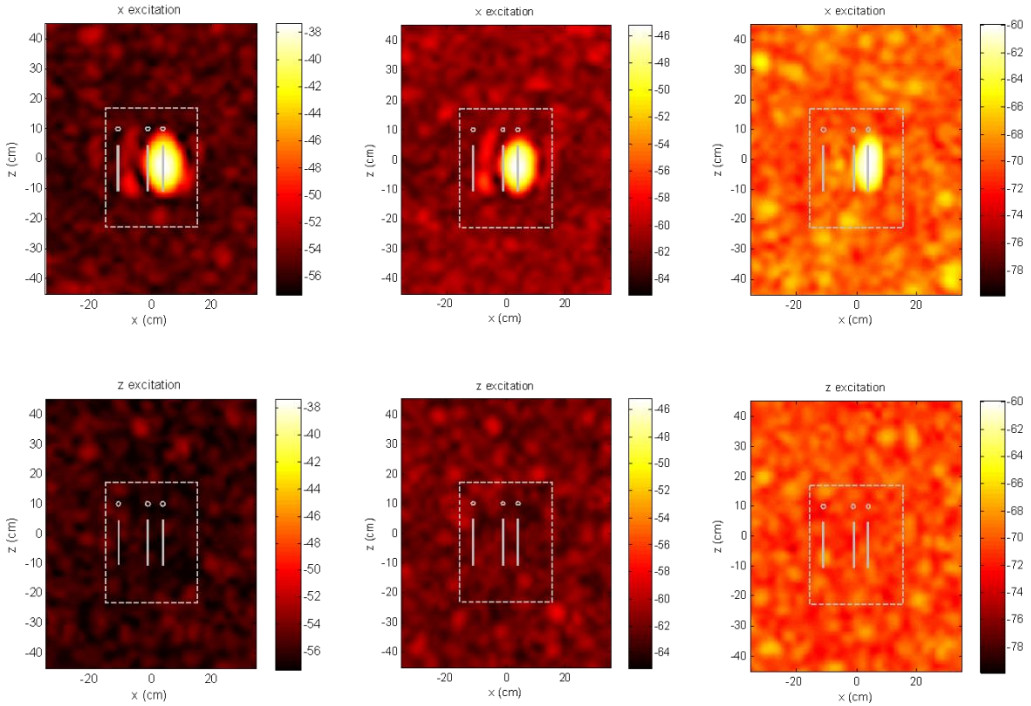


Figure 26 : Transmission-based images of the slotted box in Figure 25. Results for two polarizations of the impinging wavefronts (top and bottom row), for B_e equal to 1 GHz, 312 MHz and 62 MHz, central frequency 2 GHz. The contour of the box and the slots is superimposed on the results.

The other two columns of Figure 26 show how these results are modified when a narrower bandwidth is used for the temporal evolution of the test wavefronts. Substantially, the resolution is not affected. The main effect is the reduction of contrast between the slot image and the background. This reduction may become an issue if it passes below 6 dB, as at that point random fluctuations could be misinterpreted as apertures in the shield.

1.5 Final considerations

This chapter has discussed the main reasons why diffusive media are usually considered as adverse to signal transmissions and wave propagation. It is all the more fitting that when excited by time-reversed signals these same media appear as approaching the behavior of free-space environments.

This seemingly paradoxical observation has been explained by means of a self-averaging mechanism, proper to time reversal applied to diffusive media, as long as they present relatively narrow coherence bandwidths, i.e., reverberation and time spread.

Of the two groups of applications discussed, generalized time reversal is perhaps the most striking, since it seems to possess all the advantages of reverberation chambers (e.g., energy efficiency) and of anechoic ones (free-space-like propagation). In fact, what is actually surprising is the access it gives to a whole group of new properties, as the possibility of generating arbitrary wavefronts propagating along any direction just by changing a single excitation signal on one antenna.

The application of these properties to shield imaging is a good illustration of the reasons why time-reversal excitation of diffusive media is a promising field of research, since it would have been infeasible in neither anechoic nor reverberating chambers.

References

- [1] M. Schroeder, “Statistical parameters of the frequency response curves of large rooms,” *J. Audio Eng. Soc.*, vol. 35, no. 5, pp. 299–305, 1987.
- [2] H. Kuttruff, *Room acoustics*. Taylor & Francis, 2000.
- [3] R. Vaughan and J. B. Andersen, *Channels, propagation and antennas for mobile communications*. Institution of Electrical Engineers, 2003.
- [4] A. Ishimaru, *Wave propagation and scattering in random media*. Wiley-IEEE Press, 1999, vol. 12.
- [5] J. W. Goodman, *Statistical optics*. John Wiley & Sons, 2015.

- [6] P. Clemmow, *The plane wave spectrum representation of electromagnetic fields*. Pergamon Press (Oxford and New York), 1966.
- [7] T. Lehman, "A statistical theory of electromagnetic fields in complex cavities," *Interaction Notes, Note 494*, 1993.
- [8] D. Hill, "Electromagnetic Theory of Reverberation Chambers," National Institute of Standards and Technology, Tech. Rep., 1998.
- [9] R. Waterhouse, "Statistical properties of reverberant sound fields," *J. Acoust. Soc. Am.*, vol. 35, p. 1894, 1963.
- [10] R. V. Waterhouse, "Statistical properties of reverberant sound fields," *The Journal of the Acoustical Society of America*, vol. 43, p. 1436, 1968.
- [11] J. Davy, "The relative variance of the transmission function of a reverberation room," *Journal of Sound and Vibration*, vol. 77, no. 4, pp. 455–479, 1981.
- [12] R. Langley and A. Brown, "The ensemble statistics of the energy of a random system subjected to harmonic excitation," *Journal of Sound and Vibration*, vol. 275, no. 3-5, pp. 823–846, 2004.
- [13] K. S. Stowe, *Introduction to statistical mechanics and thermodynamics*. Wiley New York, 1984.
- [14] A. Cozza, "The Role of Losses in the Definition of the Overmoded Condition for Reverberation Chambers and Their Statistics," *IEEE Transactions on Electromagnetic Compatibility*, no. 53, pp. 296–307, 2010.
- [15] J. Philibert, "One and a half century of diffusion: Fick, einstein, before and beyond," *Diffusion Fundamentals*, vol. 4, no. 6, pp. 1–19, 2006.
- [16] D. Hill and J. Ladbury, "Spatial-correlation functions of fields and energy density in a reverberation chamber," *IEEE Transactions on Electromagnetic Compatibility*, vol. 44, no. 1, pp. 95–101, 2002.
- [17] A. Derode, P. Roux, and M. Fink, "Robust acoustic time reversal with high-order multiple scattering," *Physical Review Letters*, vol. 75, no. 23, pp. 4206–4209, 1995.

- [18] A. Derode, A. Tourin, and M. Fink, "Random multiple scattering of ultrasound. II. Is time reversal a self-averaging process?" *Physical Review E*, vol. 64, no. 3, p. 36606, 2001.
- [19] A. Derode, A. Tourin, J. de Rosny, M. Tanter, S. Yon, and M. Fink, "Taking advantage of multiple scattering to communicate with time-reversal antennas," *Physical Review Letters*, vol. 90, no. 1, p. 14301, 2003.
- [20] C. Draeger, J. Aime, and M. Fink, "One-channel time-reversal in chaotic cavities: Experimental results," *The Journal of the Acoustical Society of America*, vol. 105, p. 618, 1999.
- [21] M. Fink and C. Prada, "Acoustic time-reversal mirrors," *Inverse Problems*, vol. 17, p. R1, 2001.
- [22] M. Born and E. Wolf, "Principles of opticspergamon press," *New York*, 1980.
- [23] R. Collins and F. Zucker, *Antenna Theory*. McGraw-Hill, New York, 1969.
- [24] A. Cozza, "Statistics of the performance of time reversal in a lossy reverberating medium," *Physical Review E*, vol. 80, no. 5, p. 056604, 2009.
- [25] A. Cozza and F. Monsef, "Multiple-source time-reversal transmissions in random media," *Antennas and Propagation, IEEE Transactions on*, vol. 62, no. 8, pp. 4269–4281, Aug 2014.
- [26] H. Vallon, A. Cozza, F. Monsef, and A. Chauchat, "Time-reversed excitation of reverberation chambers: Improving efficiency and reliability in the generation of radiated stress," *Electromagnetic Compatibility, IEEE Transactions on*, vol. PP, no. 99, pp. 1–7, 2016.
- [27] K. Sarabandi, I. Koh, and M. Casciato, "Demonstration of time reversal methods in a multi-path environment," in *IEEE Antennas and Propagation Society International Symposium*, vol. 4. IEEE, 2004, pp. 4436–4439.
- [28] P. Kyritsi and G. Papanicolaou, "One-bit time reversal for wlan applications," in *PIMRC 2005*, vol. 1. IEEE, 2005, pp. 532–536.
- [29] R. Qiu, C. Zhou, N. Guo, and J. Zhang, "Time reversal with MISO for ultrawideband communications: Experimental results," *Antennas and Wireless Propagation Letters, IEEE*, vol. 5, no. 1, pp. 269–273, Dec 2006.

- [30] H. T. Nguyen, J. B. Andersen, G. F. Pedersen, P. Kyritsi, and P. C. F. Eggers, "Time reversal in wireless communications: A measurement-based investigation," *Wireless Communications, IEEE Transactions on*, vol. 5, no. 8, pp. 2242–2252, 2006.
- [31] P. Pajusco and P. Pagani, "On the use of uniform circular arrays for characterizing uwb time reversal," *Antennas and Propagation, IEEE Transactions on*, vol. 57, no. 1, pp. 102–109, 2009.
- [32] I. Vellekoop, A. Lagendijk, and A. Mosk, "Exploiting disorder for perfect focusing," *Nature Photonics*, vol. 4, no. 5, pp. 320–322, 2010.
- [33] A. Cozza and H. Moussa, "Enforcing deterministic polarisation in a reverberating environment," *Electronics Letters*, vol. 45, no. 25, pp. 1299–1301, 2009.
- [34] D. Hill, "Electronic mode stirring for reverberation chambers," *Electromagnetic Compatibility, IEEE Transactions on*, vol. 36, no. 4, pp. 294–299, Nov 1994.
- [35] H.-J. Stöckmann, *Quantum chaos: an introduction*. Cambridge university press, 2006.
- [36] A. Cozza and H. Moussa, "Polarization selectivity for pulsed fields in a reverberation chamber," in *2010 Asia-Pacific Symposium on Electromagnetic Compatibility (APEMC)*. IEEE, 2010, pp. 574–577.
- [37] A. Cozza, "Increasing peak-field generation efficiency of reverberation chamber," *Electronics Letters*, vol. 46, no. 1, pp. 38–39, 2010.
- [38] C. Draeger and M. Fink, "One-channel time-reversal in chaotic cavities: Theoretical limits," *The Journal of the Acoustical Society of America*, vol. 105, p. 611, 1999.
- [39] H. Moussa, A. Cozza, and M. Cauterman, "Directive wavefronts inside a time reversal electromagnetic chamber," in *Electromagnetic Compatibility, 2009. EMC 2009. IEEE International Symposium on*, Aug 2009, pp. 159–164.
- [40] C. Oestges, A. Kim, G. Papanicolaou, and A. Paulraj, "Characterization of space-time focusing in time-reversed random fields," *IEEE Transactions on Antennas and Propagation*, vol. 53, no. 1, pp. 283 – 293, 2005.

- [41] R. Harrington, *Time-Harmonic Electromagnetic Fields*. McGraw-Hill, New York, NY, 1961.
- [42] A. Cozza, “Emulating an anechoic environment in a wave-diffusive medium through an extended time-reversal approach,” *Antennas and Propagation, IEEE Transactions on*, vol. 60, no. 8, pp. 3838–3852, 2012.
- [43] J. de Rosny and M. Fink, “Overcoming the diffraction limit in wave physics using a time-reversal mirror and a novel acoustic sink,” *Physical review letters*, vol. 89, no. 12, p. 124301, 2002.
- [44] C. Prada and M. Fink, “Eigenmodes of the time reversal operator: A solution to selective focusing in multiple-target media,” *Wave Motion*, vol. 20, no. 2, pp. 151–163, 1994.
- [45] C. Prada, J.-L. Thomas, and M. Fink, “The iterative time reversal process: Analysis of the convergence,” *The Journal of the Acoustical Society of America*, vol. 97, no. 1, pp. 62–71, 1995.
- [46] A. Cozza and F. Monsef, “Layered electric-current approximations of cylindrical sources,” *Wave Motion*, 2016, accepted for publication.
- [47] A. Cozza, F. Masciovecchio, C. Dorgan, M. Serhir, F. Monsef, and D. Leconte, “A dielectric low-perturbation field scanner for sensitive environments,” *Antennas and Propagation, IEEE Transactions on*, 2016, under review.
- [48] T. Hansen and A. D. Yaghjian, *Plane-wave theory of time-domain fields*. IEEE Press, 1999.